



Three-dimensional nanoscale characterisation of materials by atom probe tomography

Arun Devaraj, Daniel E. Perea, Jia Liu, Lyle M. Gordon, Ty. J. Prosa, Pritesh Parikh, David R. Diercks, Subhashish Meher, R. Prakash Kolli, Ying Shirley Meng & Suntharampillai Thevuthasan

To cite this article: Arun Devaraj, Daniel E. Perea, Jia Liu, Lyle M. Gordon, Ty. J. Prosa, Pritesh Parikh, David R. Diercks, Subhashish Meher, R. Prakash Kolli, Ying Shirley Meng & Suntharampillai Thevuthasan (2017): Three-dimensional nanoscale characterisation of materials by atom probe tomography, International Materials Reviews, DOI: [10.1080/09506608.2016.1270728](https://doi.org/10.1080/09506608.2016.1270728)

To link to this article: <http://dx.doi.org/10.1080/09506608.2016.1270728>



Published online: 26 Jan 2017.



Submit your article to this journal [↗](#)



Article views: 11



View related articles [↗](#)



View Crossmark data [↗](#)

FULL CRITICAL REVIEW

Three-dimensional nanoscale characterisation of materials by atom probe tomography

Arun Devaraj^a, Daniel E. Perea^b, Jia Liu^b, Lyle M. Gordon^b, Ty. J. Prosa^c, Pritesh Parikh^d, David R. Diercks^{ib e}, Subhashish Meher^f, R. Prakash Kolli^{id g}, Ying Shirley Meng^d and Suntharampillai Thevuthasan^h

^aPhysical and Computational Sciences Directorate, Pacific Northwest National Laboratory, Richland, WA, USA; ^bEnvironmental Molecular Sciences Laboratory, Pacific Northwest National Laboratory, Richland, WA, USA; ^cCAMECA Instruments, Madison, WI, USA; ^dLaboratory of Energy Storage and Conversion, Department of NanoEngineering, University of California, San Diego, CA, USA; ^eColorado Center for Advanced Ceramics, Department of Metallurgical and Materials Engineering, Colorado School of Mines, Golden, CO, USA; ^fMaterials Science and Engineering Department, Idaho National Laboratory, Idaho Falls, ID, USA; ^gDepartment of Materials Science and Engineering, University of Maryland, College Park, MD, USA; ^hQatar Environment and Energy Research Institute, Qatar Foundation, Doha, Qatar

ABSTRACT

The development of three-dimensional (3-D), characterisation techniques with high spatial and mass resolution is crucial for understanding and developing advanced materials for many engineering applications as well as for understanding natural materials. In recent decades, atom probe tomography (APT), which combines a point projection microscope and time-of-flight mass spectrometer, has evolved to be an excellent characterisation technique capable of providing 3-D nanoscale characterisation of materials with sub-nanometer scale spatial resolution, with equal sensitivity for all elements. This review discusses the current state, as of APT instrumentation, new developments in sample preparation methods, experimental procedures for different material classes, reconstruction of APT results, the current status of correlative microscopy, and application of APT for microstructural characterisation in established scientific areas like structural materials as well as new applications in semiconducting nanowires, semiconductor devices, battery materials, catalyst materials, geological materials, and biological materials. Finally, a brief perspective is given regarding the future of APT.

ARTICLE HISTORY

Received 24 March 2016
Accepted 27 October 2016

KEYWORDS

Atom probe tomography;
characterisation;
microstructure

Introduction

The dream of every material scientist studying structure–property relationships of materials is to know exactly where each atom is located in a material and understand how that influences the various properties exhibited by it. To achieve this dream, atomic-scale characterisation techniques are vital. At present, there is still no single technique that can precisely image the exact location of all atoms in a material. However, a number of techniques are approaching this target. Atom probe tomography (APT) is one such technique that is rapidly evolving towards this target with its ~0.2 nm spatial resolution in 3-D and mass sensitivity of a few ppm.

APT was invented by Müller, Panitz, and McLane in 1967 at Pennsylvania State University [1]. APT technology has come a long way from its early days of atom probe field ion microscopes (FIMs). It has progressed through, one-dimensional (1-D) atom probes, imaging atom probes, the advent of ultrafast laser pulsing, the development of modern sample preparation methods, and the development of advanced data

analysis techniques including APT simulations [1]. The history of developments, over the last 48 years, in atom probe instrumentation is discussed in depth in various review publications and books related to APT [2–13]. Currently, the most commonly used atom probe systems are based on the local electrode atom probe (LEAP) design [14]. In this review article, we have specifically focused on giving a summary of the work currently reported from many of the operating atom probe systems as of the year 2016. Currently, there are more than 100 APT instruments around the world. As a result of the past acquisitions of Oxford Scientific by Imago Scientific and then Imago Scientific by Cameca Instruments, only commercial APT systems are now manufactured by Cameca Instruments.

APT has been rapidly adopted as a mainstream characterisation capability within a variety of scientific fields, as is evident from the rapid surge in publications based on APT (Figure 1). Among the 2500+ peer-reviewed publications related to APT, a vast majority are for understanding microstructure in metals and alloys. A significant portion of them is also dedicated

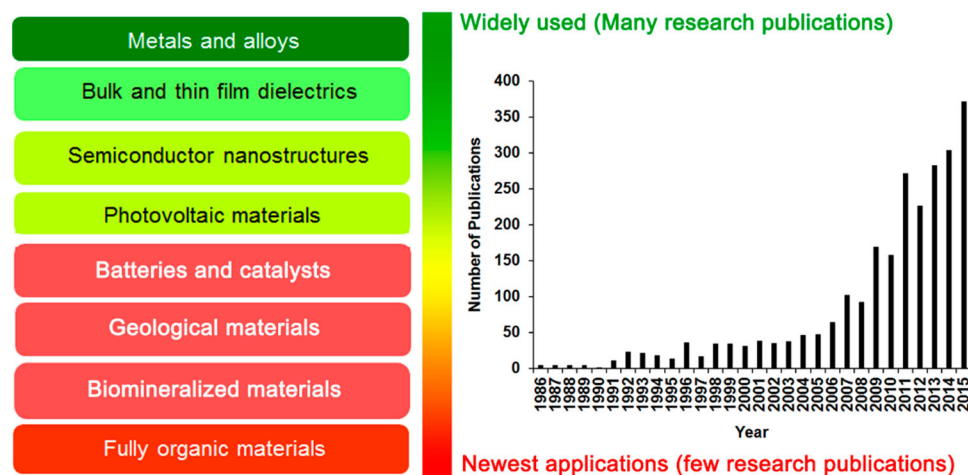


Figure 1. Examples of different application areas for APT, coloured based on the number of research publications. Green indicates many publications and red indicates only a few. The publication numbers were obtained from Web of Science for the following key words: APT, 3-DAP, APFIM, atom probe microscopy or atom probe.

to bulk and thin film dielectric materials. Analysis of semiconducting nanostructures by APT has also been increasing rapidly, leading multiple semiconductor device manufacturing companies to explore the use of APT to characterise the new generation of semiconductor devices. APT has been very successfully used for estimating dopant concentration and distribution in semiconductor nanostructures such as nanowires (NWs). APT has also been adopted for the characterisation of buried interfaces in photovoltaic materials. In parallel to these somewhat established applications, APT is constantly being applied to new areas; some key new applications include quantifying compositional homogeneity or heterogeneity in energy storage and conversion materials, such as Li-ion battery electrodes and catalyst materials; geological materials, including both terrestrial and extraterrestrial materials; biomineralised materials like animal teeth; and elephant tusks. The least explored area is the application of APT for high spatial resolution characterisation of fully organic materials, which is currently the focus of a few APT research groups across the world, including ETH Zurich, the University of Michigan, and Pacific Northwest National Laboratory (PNNL). These applications are discussed in detail in the section on application of APT to materials. Before delving into various applications, a brief review is provided on the broad classification of currently operational APT systems, novel sample preparation methods, APT experimental procedures, data reconstruction, analysis and correlative APT-TEM, and other microscopy techniques.

Current status of APT instrumentation in 2016

Multiple types of APT instrumentation are currently used around the world for routine microstructural

characterisation. An attempt is made here to provide some broad classification of APT instruments. The first classification is based on pulsed voltage APT *v.* pulsed-laser-assisted APT. Pulsed voltage APT has been extensively used for electrically conductive materials; for example, microstructural characterisation of metals and alloys. The field evaporation in pulsed voltage APT is attained by a combination of a direct current (DC) standing voltage and a pulsed voltage of typically 15–25% of the standing voltage acting on a <100 nm diameter needle specimen placed very close to an open aperture electrode (local electrode). The voltage pulses on top of the standing DC voltage permit stoichiometric evaporation of elements with even widely dissimilar evaporation fields. In laser-pulsed APT, an ultrafast pulsed laser (picosecond or femtosecond pulse), focused on the apex of the specimen along with a DC standing voltage, is used for inducing ion evaporation. Starting from pioneering work by Tsong and Kellogg in late 1970s, the implementation of pulsed lasers opened the application areas of APT beyond conductive metals and alloys, permitting APT analysis of semiconducting and dielectric materials [15,16]. There has been extensive application of laser-pulsed APT to analyse dielectrics, semiconductors, and even organic and geological materials in recent times.

The laser-pulsed APT is further classified based on the wavelength of laser used. Earlier versions of laser-assisted APT systems used a 1064 nm wavelength neodymium-doped Yttrium aluminium garnet (Nd:YAG) infrared laser. The Cameca LEAP 3000 series APT instruments use a frequency doubled 535 nm green laser. More recently, Cameca LEAP 4000 series APT instruments use a diffraction-limited focused frequency-tripled 355 nm wavelength Nd:YVO₄ ultra-violet (UV) laser. The photo of CAMECA LEAP4000XHR APT system in Environmental Molecular Sciences Laboratory, PNNL is given in Figure

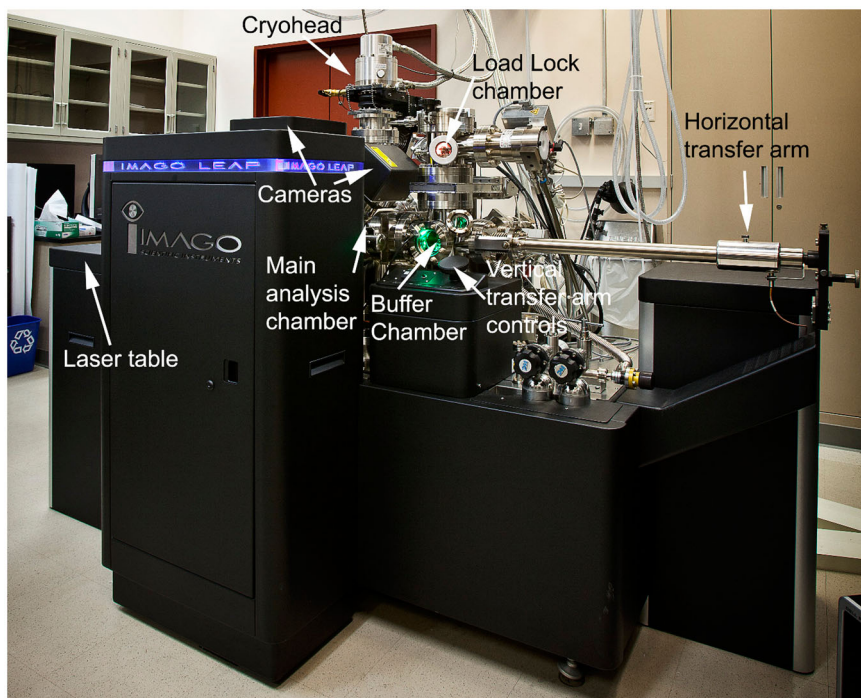


Figure 2. The CAMECA LEAP4000XHR APT system in Environmental Molecular Sciences Laboratory, Pacific Northwest National Laboratory.

2 with some important parts of the instrument labelled. Some laser-assisted wide angle tomographic atom probe systems are also in use in a few research groups around the world, offering tuneable wavelength systems capable of switching between pulsed infrared (1080 nm), green, and UV. One of the reasons to go to smaller laser wavelength is the resultant reduction in laser absorption depth, which helps reduce the size of the laser-heated volume on the specimen; this directly translates to faster heating and cooling rates and improved mass resolving power. In addition to these commercial systems, there are other home-built APT systems still operating in some universities around the world, for example, the APT systems operating at the National Institute for Materials Science in Japan, [17] the University of Munster [18], and the University of Rouen [19].

Another classification is based on whether the instrument has an energy compensating reflectron lens or a straight flight path. Reflectron lenses were incorporated in atom probe systems to facilitate energy compensation and improve the mass resolution [20–22].

A final classification is based on the type of detector used. Almost all the current generations of atom probe systems use a delay line detector, coupled with a microchannel plate, for position sensing and time-of-flight estimation of field evaporated ions from the specimen [23]. More recently, the Cameca LEAP 5000 APT was launched, which uses a UV laser with an improved detector for much higher detection efficiency [reference: Cameca LEAP 5000 release notes].

Specimen preparation

From the earliest development of APT instruments, an array of conventional specimen preparation methods, including electropolishing and cleaving, existed for preparing samples of conductive materials. For non-conductive materials, methods included cleaving or dip-coating if polymers were utilised. These traditional methods are covered fairly extensively in various text books available on APT [24,25]. However, over the last two decades, an array of new techniques came into existence for APT needle-specimen preparation; these are the focus of this section.

Focused ion beam-based lift-out process

When focused ion beam (FIB) systems became commercialised for use in material science, a new method of fabricating specimens for APT analysis came into existence [26]. Using a FIB scanning electron microscope (SEM), a small cantilever of the specimen to be analysed could be cut and transferred onto a microtip array, which is a prefabricated silicon wafer with approximately 100 μm tall posts with an end diameter of 2 μm [27]. Small sections of the specimen are attached to individual posts using an *in situ* beam-assisted vapour deposition. The triangular wedge specimens are annular milled first with high acceleration voltage (30 kV) Ga ion beam for shaping, then with a lower acceleration voltage (2–5 kV) for final sharpening to obtain final APT specimens with less than 100 nm tip diameter and very low Ga implantation

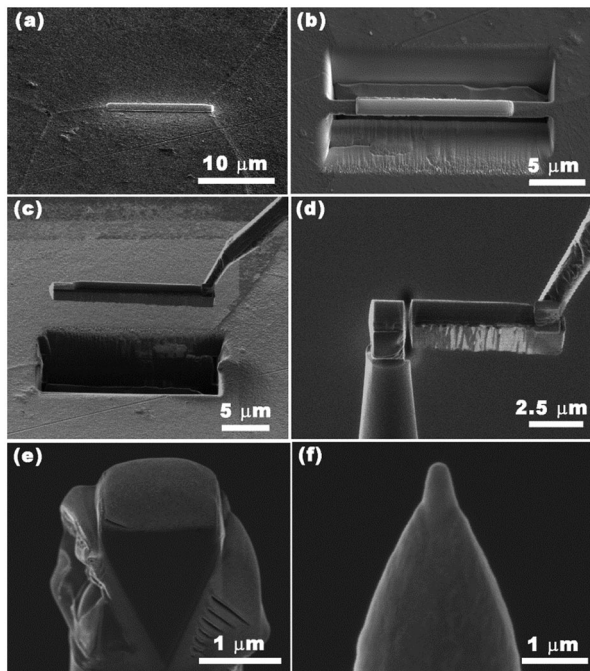


Figure 3. FIB-based lift-out process and annular milling for needle sample preparation: (a) selection of a specific site for lift-out sample preparation and Pt capping of the ROI; (b) trenching on either side of the ROI to get a triangular wedge; (c) lift-out of the specimen using a nanomanipulator; (d) attachment of a specimen wedge on the microtip post; (e) one specimen wedge on the microtip post at the beginning of annular milling; (f) final needle specimen with <100 nm end diameter [Image courtesy Arun Devaraj, Pacific Northwest National Laboratory (PNNL)].

[28]. An example of a FIB lift-out method for specimen fabrication is provided in Figure 3.

Often the subject of interest for APT analysis is an interface between two phases or between grain boundaries of the same phase. In multicomponent alloys, the nanoscale segregation of alloying elements to grain boundaries can directly influence the final properties of the alloy. In order to analyse such localised features with APT, a site-specific lift-out process is used: using a dual beam FIB SEM, a precise site is identified, protected with Pt capping, and then lifted out and attached to a microtip array using a procedure similar to a

general FIB lift-out. During annular milling of the attached wedges of the specimen, special care is taken to identify and retain the interface within 100 nm of the APT specimen apex. This procedure can also be integrated with electron backscatter diffraction (EBSD) to identify specific regions of interest for APT analysis to conduct site-specific sample preparation.

APT specimen preparation of thin films

When analysing thin films on substrates, especially when there is a significant difference in the field evaporation behaviour of the film and substrate, both the yield and accuracy of results can be problematic if specimens are analysed only in normal orientation. This is mainly due to the possibility of having trajectory aberration right at the interface of the thin film and substrate. Often, in order to verify the role of such aberration in final data interpretation and analysis, samples need to be prepared in rotated geometries. The rotation of the sample wedge helps to align the interface between the thin film and substrate at any angle to the axis of the needle specimen, which can improve yield in some cases, and possibly improve reconstruction accuracy. Sometimes, analysis is also attempted on the same specimen in bottom-up orientation after 180° rotation of the lift-out wedge from the specimen. Analysing rotated samples permits independent study of the influence of sample geometry on final APT results and thus improves the overall reliability of the interpretation of APT data. Figure 4 illustrates the sample preparation process of rotating a FIB lift-out wedge by 90° before attaching on the microtip and then annular milling. Specifically, it is a CeO₂-ZrO₂ multilayer stack with total thickness of 140 nm on a (0001) sapphire substrate [29].

Lift-out-based preparation of nanoparticles

Many of the advanced engineering materials of current and future research interest for energy and

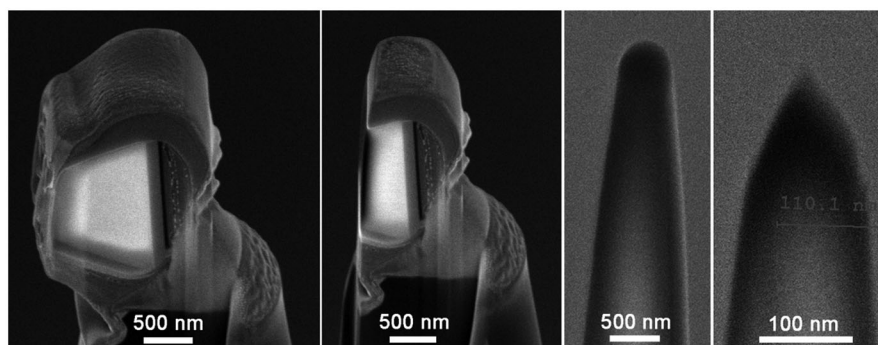


Figure 4. Transverse specimen preparation: the lift-out wedge is rotated 90° before attaching to the microtip array and then annular milling (Image courtesy A. Devaraj, PNNL).

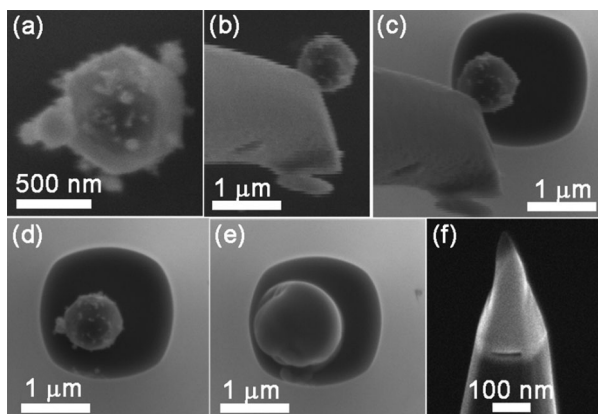


Figure 5. APT sample preparation of LiMnO_2 nanoparticles [30]. (a) SEM image of the ~ 500 nm diameter LiMnO_2 nanoparticle; (b) electrostatic lift-out of a nanoparticle by nanomanipulator; (c) transfer of the nanoparticle onto a microtip array needle; (d) the transferred nanoparticle on top of the microtip array specimen post; (e) nanoparticle after electron beam-assisted Pt deposition; (f) final needle specimen after annular milling (Image courtesy A. Devaraj, PNNL).

environmental applications are in the form of nanoparticles with sizes from a few to hundreds of nanometres. Preparing APT specimens of such nanoparticles is a significant challenge because their small size limits the manipulability of the particles. A modification of the conventional lift-out method can be used for nanoparticles larger than 100 nm: after dispersing the nanoparticles on a clean silicon wafer substrate, the nanomanipulator can be used to attract some of the particles electrostatically and transfer them onto a silicon microtip array. Once the nanoparticles are placed on the microtip, they are coated using electron beam-assisted platinum deposition to protect them from ion beam implantation damage. All manipulation up to this stage is done using electron beam imaging. Subsequently, using low ion-beam currents, the specimen is precisely annular milled to achieve the final dimensions suitable for APT analysis. If side cavities are observed between the nanoparticle and the microtip array, additional electron beam-assisted Pt deposition can be applied from the sides to fill the void. An example of this method of preparing APT specimens

from nanoparticles is provided in Figure 5 [30]. Other methods for preparation of APT specimens of nanoparticles include encapsulation of nanoparticles using atomic layer deposition (ALD), [31] dielectrophoresis [32], and agglomerate lift-out [33].

APT-TEM correlation specimen preparation

As will be discussed in more detail in section 5, the correlation of APT results with those of other techniques, particularly transmission electron microscopy (TEM), can provide significant complementary information. However, this correlative work requires some modifications to the specimen preparation process. The main distinction from what has been previously described is that the specimen needle or array must be compatible with a TEM holder. Specimens for APT-TEM correlative microscopy can be fabricated as wire specimens [34–38], as lift-outs onto a single specimen holder made of an electropolished metal wire [39–41], or onto an electropolished or FIB-prepared metal (Cu, Ni, Mo, Au) mesh or silicon half-grids [39,41,42]. For lift-out methods, the metal or silicon projections are prepared such that they have an end diameter of a few micrometres. A FIB-prepared wedge of the specimen can be attached to each such post, then polished using annular milling. Avoiding any additional protrusions within several microns of the apex of the tip will foster successful APT analysis and TEM imaging. APT-TEM correlative microscopy specimens, prepared in this manner, can be imaged in a TEM both before and after interrupted APT analysis to understand both initial and evolved tip shape after partial field evaporation. Such post-APT analysis imaging of APT specimens of complex heterogeneous materials can help in understanding the field evaporation behaviour and resultant aberrations due to local magnification artefacts. TEM-APT direct correlation also aids in understanding the extent of evaporated volume, which aids in generating accurate reconstructions. An example of APT-TEM correlative specimen preparation onto a Cu grid is given in Figure 6. Figure 6 (a) and (b) are taken from Gorman *et al.*, [39]

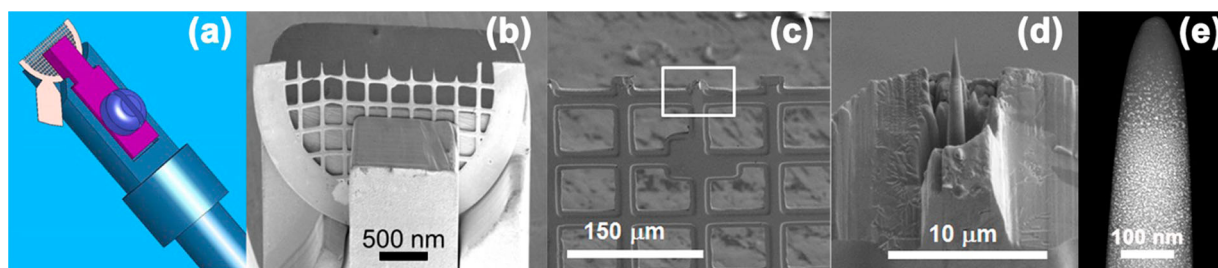


Figure 6. (a) Schematic of a holder facilitating direct coupling of TEM and APT (b) a low magnification SEM image of the half Cu grid in the holder (c, d) magnified SEM images showing location of a single needle sample. (e) a scanning transmission electron microscope image of a single APT needle specimen (Figure (a) and (b) adapted from B. P. Gorman *et al.*, [39] (c–d) images courtesy A. Devaraj, PNNL).

providing a schematic of the Hummingbird Scientific APT–TEM holder (Figure 6(a)) and low magnification SEM image of the Cu half-grid in the Hummingbird Scientific holder (Figure 6(b)). A fabricated APT needle specimen on the Cu half-grid is shown in Figure 6(c), where the location of the needle specimen is highlighted by a white rectangle. The specific needle specimen is shown in Figure 6(d). A STEM image of the needle specimen is provided in Figure 6(e). This sample holder can be loaded both into the TEM and directly into an APT specimen puck.

Preparation of nanowire specimens for APT analysis

NWs synthesised by the vapour–liquid–solid (VLS) growth mechanism [43] have dominated fundamental research studies since the early 2000s. The popularity of studying VLS-grown NWs is arguably due to the *in situ* control of composition and morphology, leading to NWs of controlled dopant type with both radial and axial functional interfaces [44]. The intrinsic, needle-like shape and nanometre scale diameter (10s–100s of nanometres) of semiconductor NWs makes them ideal specimens for APT analysis using a LEAP. Two general strategies have been developed to prepare specimens: in one, NWs are synthesised bottom-up in patterned arrays to allow a systematic indexing of positions, while another way makes use of a FIB lift-out approach to mechanically position an individual pre-grown NW on prefabricated microposts. Choice of the specimen preparation approach should be made based on the availability of the required tools and time requirements of the different techniques.

The first demonstration of APT analysis of an individual VLS-grown NW was performed by Perea *et al.* [45] Au catalyst discs were patterned by electron beam lithography and metal deposition, from which arrays of vertically epitaxial InAs NWs were grown directly on flat GaAs(111) substrates (Figure 7(a)). Since the small NW diameters are below the diffraction limit of the optical charge-coupled device cameras of the LEAP, it is a challenge to ‘see’ them for alignment, and thus a central cross pattern of closely spaced NWs acts as a visual fiducial to assist indexing. It should be noted that the integrated laser system in the LEAP 4000 and 5000 models can be used to help with NW alignment by observing the reflected laser spot.

A more facile alignment of NW specimens can be made by growing vertically epitaxial NWs on top of predefined microposts, where the microposts themselves are easily seen with the LEAP specimen alignment optics. Using a wafer dicing saw, micropost array substrates can be fabricated in series (Figure 7(b)) to create pedestals on which individual VLS-grown NWs can be grown from drop-cast Au colloid solution and analysed with APT (Figure 7(c)) [46].

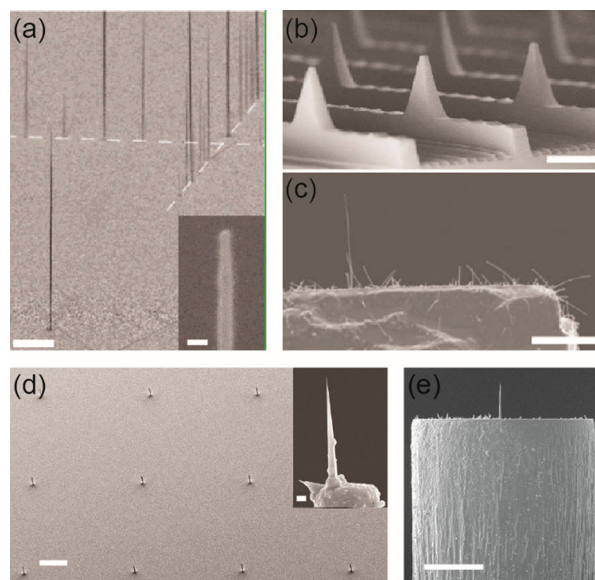


Figure 7. SEM images of various NW-patterned arrays for APT analysis. (a) InAs NWs grown in a square pattern array. Cross fiducial pattern is outlined with dashed line. Scale bar is 20 μm . The inset shows the foreground NW tip. Scale bar is 50 nm. Images adapted from Perea *et al.* [45] (b) Microposts of Si(111) produced by a wafer dicing saw. Scale bar is 100 μm . (c) Silicon NW grown epitaxially from drop-cast Au colloid on posts shown in (b). Scale bar is 5 μm . Images adapted from Perea *et al.* [46] (d) Micropost array produced by micro-fabrication methods used for the epitaxial growth of semiconductor NWs. Scale bar is 2 μm . The inset shows a micropillar with two Au islands on top used to catalyse NW growth. Images adapted from Xu *et al.* [48] (e) Single NW grown from e-beam deposited catalyst on top of microfabricated micropost. Scale bar is 15 μm . Image courtesy of D.E. Perea, PNNL.

However, the serial fabrication makes this approach very time-consuming. A more efficient method of micropost fabrication is by using a photolithography and reactive ion etching approach to create arrays of microposts, atop which NWs can be directly grown (Figure 7(d)) [47,48]. However, growing only a single NW on the micropost top from drop-cast catalyst is challenging. In Figure 7(c) and (d), more than one NW is observed on the micropost, which can cause the unwanted co-field evaporation of multiple NWs. One solution to this dilemma is to mechanically remove unwanted NWs in the vicinity of the NW of interest using a nanomanipulator [48].

A more precise method to ensure the growth of a single NW per micropost is to use electron beam lithography. Electron beam lithography and metal deposition can precisely deposit pads of catalyst metal on top of the microposts to facilitate the controlled growth of a single vertically epitaxial VLS-grown NW per micropost. In Figure 7(e), a single vertical NW is observed on a micropost, ideal for APT analysis. The advantage of confining NW growth to the micropost tops is that a single NW can be grown, as opposed to the uncontrolled deposition of catalyst nanoparticles

on microposts, where multiple NWs may grow on each micropost top. Another advantage of this approach is the ability to fabricate micropost arrays with catalyst pads of varying size and composition to synthesise VLS-grown NWs of varying diameter on the same substrate, which is a facile route to studying catalyst-dependent growth kinetics.

One challenge to the APT analysis of NWs is analysis yield. The intrinsically small diameter that makes them ideal specimens for analysis also makes it a challenge to collect significant amounts of data before catastrophic specimen fracture caused by the electrostatic forces applied to initiate thermally assisted field evaporation. To increase the analysis yield of NWs grown directly on the analysis substrate, Perea *et al.* [47] described a strategy to grow the NWs with an intentionally tapered base, which seems to provide increased mechanical strength. In addition, the tapered morphology also was shown to increase the thermal conductivity of the NW, which can reduce thermal artefacts observed in the mass spectrum [47] which seem to be more relevant with using a 532 nm wavelength laser as opposed to the 355 nm wavelength laser.

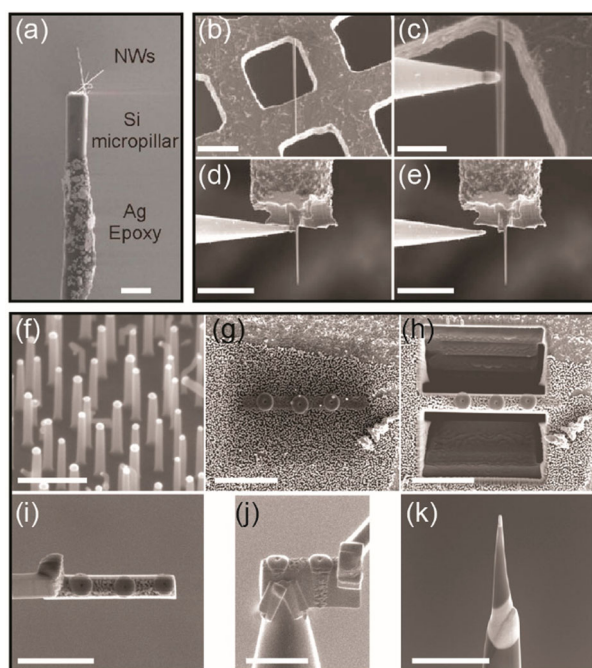


Figure 8. SEM images of FIB-based preparation of NW specimens for APT analysis. (a) A micropost mounted on a W tip with pre-grown NWs on top. Image adapted from Xu *et al.* [48] (b) Identification of NW of interest deposited ex situ on TEM grid, followed by (c) lift-out, (d) attachment, and (e) release onto micropost. Scale bars are 5 μm , 2 μm , 10 μm , and 10 μm , respectively. Images (b–e) adapted from Diercks *et al.* [49] (f) As-grown NWs on growth substrate. (g) Deposition of Pt circular markers, each centred on a single NW, followed by (h) coarse milling, (i) lift-out, (j) mounting. (k) Subsequent fine milling into needle morphology of specimen containing a single NW. Scale bars are 300 nm, 5 μm , 5 μm , 5 μm , 4 μm , and 2 μm , respectively. Images (f–k) adapted from Blumtritt *et al.* [50].

An alternative approach to the preparation of NWs for APT analysis is based on the site-specific lift-out method using a dual beam FIB–SEM equipped with a nanomanipulator system (referred to here as just FIB) [27]. Using the FIB, two general methodologies have been demonstrated. One approach is to lift out an entire microfabricated micropost with a NW grown on top and subsequently attach it to another designated micropost (Figure 8(a)) [48]. The other general FIB method is either the lift-out of NWs transferred to another substrate such as a TEM grid, [49] or the lift-out of individual NWs directly from the growth substrate [49–52] and subsequent mounting on predefined microposts. In Figure 8(b–e), the identification and lift-out of a NW deposited on a TEM grid and attachment to a micropost is demonstrated [49]. An alternative approach is to use the FIB to lift out NWs directly from the growth substrate, where the NWs are grown in a patterned array [52] or randomly [50]. In Figure 8(f–k), individual NWs are lifted out directly from the growth substrate, attached to microposts and sharpened into needles [50]. For NWs that are not grown using a catalyst particle, i.e. not VLS, such as ZnO NWs, controlled growth of single NWs on microposts poses a challenge. So the FIB-based approach to specimen preparation has been shown to be a practical method [53]. Whereas the above methods enable the analysis of NWs in an axial orientation, Mangelinck *et al.* demonstrated radial analysis enabled by the FIB lift-out of NWs that were transferred to substrates and over-coated with a metal film [54].

APT experimental procedures and data reconstruction

Experimental procedures

APT experimental procedures have evolved over the years, especially with the standardisation and commercialisation of available technology, and they continue to evolve today. Many of the manual operations summarised by M.K. Miller in 2000 [24] have become standard and automated, yet the number of analysis parameters and the growing variety of analysable materials have encouraged continued evolution in experimental design. Advanced computer control enables complex instrument control; steady advances in acquisition field-of-view (towards capturing all ions departing from a specimen), together with the ability to monitor ion evaporation statistics in real-time, have promoted improved analysis yield and data quality. Today, automation is generally limited to variation of specimen voltage to maintain target ionisation rates and laser positioning to maintain optimised alignment to the specimen in pulsed-laser mode. Detection rate (DR) targets and other analysis parameters can be changed

during acquisition, but this must be done manually by the user.

Relevant APT experimental design is mostly discussed in recent books [24,25,55]. A few papers specifically address issues related to proper selection and evaluation of analysis conditions [56–63], but in general, discussions beyond listing the actual experimental parameters used for a particular study are beyond the scope of a majority of the peer-reviewed literature. We have tried to capture the essential spirit and experimental details contained in the relevant published literature in this section.

One component of experimental design is determining the combination of analysis parameters that achieves the desired analysis objectives. Ideally, an APT experiment extracts data from a material with optimum quality and minimum analysis time. Because each specimen may be unique, and all material types do not perform similarly under equivalent APT analysis conditions, the user is often required to choose control parameters that properly balance data quality, analysis time, and analysis yield. Understanding these trade-offs may require analysis of a ‘standard’ material with well-characterised composition and microstructure to properly evaluate the accuracy of the APT data.

Voltage-pulsed APT analysis has a long history, and analysis parameter selection procedures have been developed with the primary aim of ensuring accurate composition measurements. The primary analysis parameters include specimen base temperature (T), ion DR , pulse frequency (f), and pulse fraction (PF). Proper experimental design requires specimens to be first made of appropriate shape and dimensions with the target region-of-interest (ROI) centred in, and near the apex of, the sharp needle (see previous section). Then in principle, it is just a matter of estimating either the number of ions necessary to analyse through the ROI or monitoring the live analysis (1-D and 2-D composition evolution) to decide when the experiment is complete (ignoring analysis yield considerations for the moment).

There are a number of metrics which can be considered when evaluating valid analysis parameter selection. These metrics are based on the quality of the chemical information (mass spectrum), spatial information, and analysis yield. Measurable aspects of the mass spectrum include the peak shapes (mass resolving power or MRP), number of peaks or charge states, number of complex ion species, background, and numbers of background-related peaks (hydrides for example). Unless other defects in the acquisition are present, then metrics, such as high MRP, few peaks and charge states, few complex ions, low background, and few background-related peaks, should result in the most accurate composition determinations. Self-consistent investigations can be performed on a material to optimise these mass spectral qualities.

There are a number of recognised evaporation defects that affect compositional accuracy, and in many cases, analysis conditions exist that eliminate or minimise these effects. A good example is preferential retention of certain ion species; the evaporation field produced on the apex may cause weakly bound atoms to be preferentially evaporated and strongly bound atoms retained, skewing the composition primarily because of insufficient analysis PF . Miller and Smith analysed an Fe-3wt.%-Si steel showing how low PF and f gives inaccurately high levels of silicon [56]. Later, Miller and Russell showed that the availability of newer instrumentation with higher available f allowed for accurate analysis with lower PF [57]. Other evaporation defects which affect compositional accuracy include loss due to increased probability of multiple evaporation events occurring during a single pulse (multi-hits) [64,65], or high DR resulting in normal detector pile-up [66], occurrence of complex molecules and spectral overlaps [60,67,68], dissociation of complex molecules [69], and loss of neutral species [63].

Measurable aspects of the ion positions themselves include evaluations of the detail in field-desorption maps and short-range positional order (Fourier transforms [70] and spatial distribution maps (SDMs) [71]). Evaluation of the short-range order is ultimately tied to the quality of the 3-D reconstruction (next section).

There are common occasions where an APT experiment terminates prematurely. One occasion is when a specimen is shaped such that the cross-section at a given depth, and for selected analysis conditions, requires a voltage beyond which the instrument can supply, thus terminating the experiment. A more common occasion is when the specimen ruptures at some point during the analysis (specimen failure). This occurs when the fields necessary to establish evaporation at the specified DR result in material stresses that approach the ultimate tensile strength limit for the material and any defect in the microstructure may lead to mechanical failure [72,73].

Laser-pulsed APT has a much shorter history than voltage-pulsed APT, but it has the critical advantage that thermal-based evaporation allows for the analysis of electrical insulators as well as metals. The generally lower required evaporation-field usually offers increased specimen yield (larger datasets) which may critically impact the analysis objectives for a given study. One disadvantage is that the higher peak apex temperature and side-specimen illumination can provide added complexity to interpretation of the mass spectrum and reconstruction accuracy, and the relative immaturity of the technique means that there is less guidance in the published literature for experimental procedures.

There is some small variety in laser-pulsed APT instrumentation around the world. Parameters, such as laser spot size, wavelength, available laser pulse energy (LPE) range, and polarisation, are generally fixed

features for a given instrument model, and some consideration must be made regarding a particular instrument and optimum conditions necessary for quality APT analysis. For small-laser-spot designed instruments, like the LEAP, procedures must be incorporated to ensure continued specimen-laser alignment [55]. For instruments with multiple wavelengths and polarisation, some consideration must be made regarding the wavelength appropriate for a given application [74–78]. Nevertheless, the considerations for evaluating valid analysis parameters are the same as for voltage-pulsed APT. Before detailing the trade-offs for general parameter selection, a couple common laser-pulse considerations are worth noting.

Compositional and spatial accuracy effects occur in laser-pulsed mode similar to voltage-pulsed mode. The *LPE* effectively takes the place of *PF* in voltage-pulsed mode, and determines the temperature (field) difference between the on-and-off ion emission states of the specimen. When the difference is too small, then preferential evaporation and surface migration can occur [79] leading to a loss in both compositional and spatial accuracy. In addition, the non-uniform heating of the specimen can lead to an asymmetric tip shape and reconstruction inaccuracies [80]. Care needs to be taken to prevent preferential evaporation and minimise tip asymmetries.

Laser-pulsed mass spectra generally present more peak variability relative to voltage-pulsed APT. The laser-evaporation process may include more hydride-containing peaks as well as complex cluster ions. The

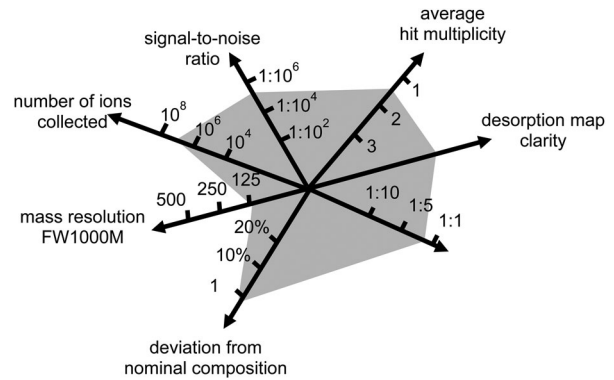


Figure 9. Diagram summarising the quality assessment of an analysis. The grey area shown in the plot is the typical optimal setting for a series of Al–Cu–Mg specimens analysed in pulsed-voltage mode with a LEAP 3000X Si (adapted from [25] courtesy of Baptiste Gault).

availability of any baseline mass spectrum can be useful for the interpretation of these more complicated mass spectra. For example, when a material yields mass spectra in both APT modes, the differing distribution of peak types for the same bulk composition can provide clues to aid in the identification of unknown peaks; however, when analysis in both APT modes is not possible, analysis of related materials with well-known compositions and impurity levels can then aid in the identification of peaks from materials with less well-known compositions.

The challenge in both acquisition modes is to attain an acceptable analysis yield (analysis volume or number of ions collected) while achieving the highest data

Table 1. General experimental parameter considerations, data quality trends and trade-offs (parameter increases ↑, trend improves +, or worsens – the metrics) (taken from [55]).

Acquisition parameter	Variable	General trend	Metrics	Comments	Primary trade-off
Pulse rate ↑	f (Hz)	++ – – –	Background m/n range Wrap around Base temperature offset effects (laser)	Faster is better Exceptions: high mass ions with long TOF or extremely poor thermal diffusivity materials in laser mode	Almost none except for practical considerations for TOF of all potential ion species
Specimen base temperature ↑	T (K)	++ – – – –	Analysis yield MRP Background Heat flow (laser) Surface diffusion	Lower leads to better spatial resolution, higher leads to better yield	Data quality vs. analysis yield
Detection rate ↑	DR (ions/pulse)	++ – – –	Background Analysis yield MRP Multi-hit performance	Faster is better Exception: poor yielding materials and materials prone to multi-hit behaviour	Data quality vs. analysis yield
Pulse fraction ↑ (voltage mode)	PF (%)	++ + – –	Compositional accuracy Background Potential for PF decay High cycle fatigue	Higher is better Exception: Extreme PF may limit MRP and pulse amplitude is hardware limited	Data quality vs. analysis yield
Laser pulse energy ↑ (laser mode)	LPE (nJ or pJ)	+++ ++ + + – –	Analysis yield Background MRP Effective pulse fraction Complex ion generation Surface migration	Higher leads to better yield Lower leads to better spatial resolution	Data quality vs. analysis yield

quality possible. As these two goals are generally opposed, the choice of experimental parameters is often an exercise in choosing various trade-offs: some aspect of data quality or analysis speed versus analysis yield [81] (see Table 1).

An APT analysis experiment might be evaluated with regard to the main aspects of the quality assessment of the experiment. Figure 9 shows a radar plot with an axis for each parameter and the quality of that metric for a given set of analysis parameters. The goal of the experiment is then to maximise the area contained within the plot (grey).

The fact of the matter is some materials/applications yield successfully under a variety of analysis conditions, enabling data collection with optimum chemical and spatial information and high information-content 3-D reconstructions. Other materials are more fragile and may only yield to a narrow set of analysis conditions. In those cases, reduced information content is available, but useful nanoscale information is often still accessible. Or at a minimum, relative differences between datasets may still be relevant as long as some level of precision is achieved.

The future of APT experimental procedure promises to add many more automated procedures, including specimen alignment and application-specific control [82]. For example, scripted experimental control has been discussed which would allow the instrument to respond based on a set of pre-programmed procedures or recipes [83]. Such automation frees the user from monitoring the acquisition and encourages optimised analysis conditions as each material type or interface is exposed during an analysis.

Reconstruction

The 3-D chemical-imaging power of APT is what sets it apart from other microscopy techniques. The process of converting detected 2-D ion positions and event order (X , Y , N) into a reassembled 3-D map approximating original atomic positions (x , y , z) is referred to as reconstruction. The current standard methodology utilises a simple model with a limited number of parameters that has evolved to accommodate increasing instrument field-of-view [84,85]. Even when the assumptions of the underlying model are not well met, reconstruction parameter choices can be made such that the known features are reproduced surprisingly well. In this section, we will briefly review the basic details of the common reconstruction protocol and discuss some of the known limitations and common best practices for achieving accurate reconstructions. For a more complete review of reconstruction, we refer the reader to a number of recent books and review articles focused on the subject [25,55,86–90].

The conventional reconstruction algorithm utilises a single-point projection onto a spherical surface [84,85].

Key inputs in the reconstruction algorithm used in the commercially available IVAS software (CAMECA Instruments, Inc.) include ionic volume, detection efficiency, image compression factor, either tip radius (initial or final) or the product of geometrical field factor (k) and evaporation field (F_e), sphere-to-cone ratio, and radial evolution procedure (voltage, shank angle, or tip profile) [55]. The detected ions are back-projected from the detector onto a single curvature (spherical) surface, one at a time, by way of a fixed projection point. The projection surface is allowed to change curvature between events, as the specimen erodes, and as prescribed by the specific radial evolution procedure selected in the software. Between events, the projection surface position is also incremented in depth (z) based on the active area of the reconstruction and the ionic volume of the previous event.

Under ideal circumstances, this approach works exceedingly well. Figure 10 shows the reconstruction for an aluminium grain with the $\langle 113 \rangle$ pole oriented nearly parallel to the specimen axes. The full periodicity of the atomic layers is observed along each pole, revealing the near-atomic resolution contained within this dataset. It is the highly ordered disassembly of the metal structure by the physics of field-evaporation that allows for the reconstructed detail observed in this example.

Although the average 3-D periodicity in this example readily matches the known crystallography, there are regions that are distorted. A combination of surface faceting (variable curvature) and ion trajectory aberrations due to localised surface topology can cause higher magnification where poles and zone lines intersect the surface [87] which are observed as regions of lower atomic density in Figure 10. Depending on the information one would like to extract from the dataset, these regions can be excluded [92], the local positions can be corrected [93–95], or the aberrations can be ignored when they have negligible impact on the results.

Inhomogeneous materials commonly have nanoscale features or interfaces between materials that have differing evaporation-fields. This can cause either small-scale or large-scale deviations from a single curvature surface introducing errors into the reconstruction. Correlative methods, such as SEM or TEM, and simulations have shown that the apex of the specimen can become highly non-spherical under these circumstances [88,96]. Nevertheless, good correlation with known feature sizes and shapes can still be achieved as demonstrated in Figure 11. In this example, the amorphous silicon, silicon oxide, and SiGe regions all require different evaporation-fields. Even though the tip shape becomes highly non-spherical during these portions of the analysis, Figure 11(c) shows good agreement between the APT reconstruction and measured feature sizes.

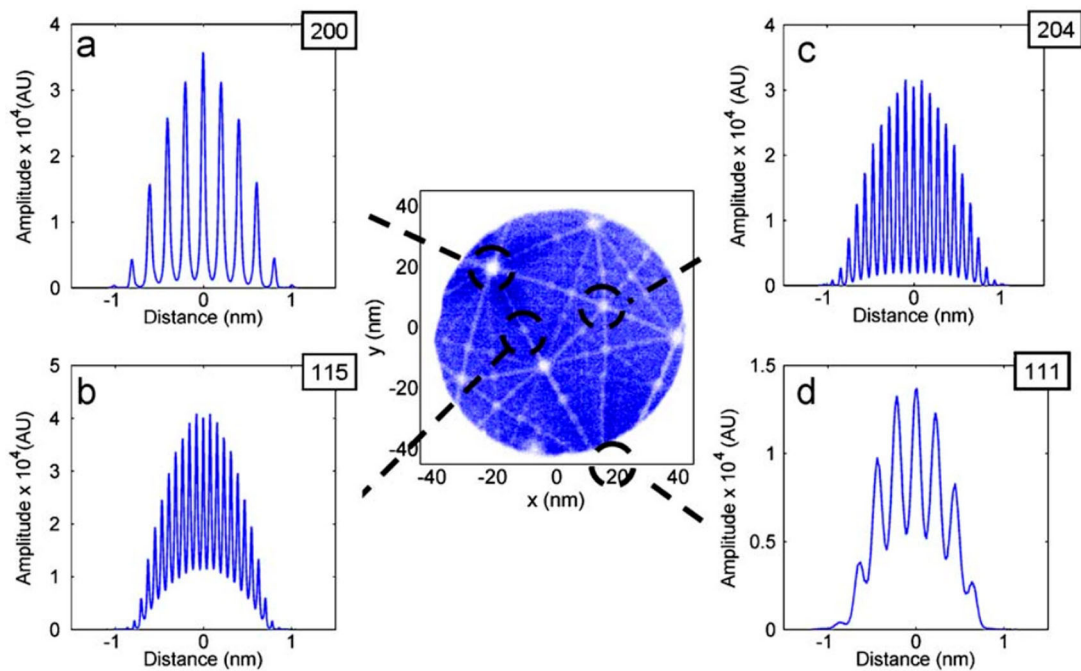


Figure 10. XY-view of the reconstruction (centre) for an aluminium specimen and the resulting SDMs along various poles observed in the reconstruction. The inter-planar spacing of the aluminium atoms along the various crystallographic directions is readily observed in the spatial distribution map (SDM) (adapted from [91]).

In order to achieve maximum precision and accuracy, reconstruction parameters need to be appropriately chosen and constrained. Investigators have reported procedures using known properties of the material (e.g. the atomic periodicity as illustrated in

Figure 10) [91,97–100], feature sizes, and relative locations as measured by microscopy (e.g. the features shown in Figure 11) [38,86,101], and APT specimen dimensions and final tip shapes after field evaporation (e.g. total eroded depth and final tip radius) [100–103]. By constraining the reconstruction adequately, reliable comparisons can be made between datasets. For example, Prosa and co-workers showed that by implementing a consistent set of reconstruction procedures, multiple analyses of an Arsenic-implant dose in Silicon could be measured with a good precision [100].

Today, the single-point projection model works surprisingly well across a broad array of structures, even when the underlying assumptions for the model are not well met. The limited number of parameters available which define the procedure are both the strength

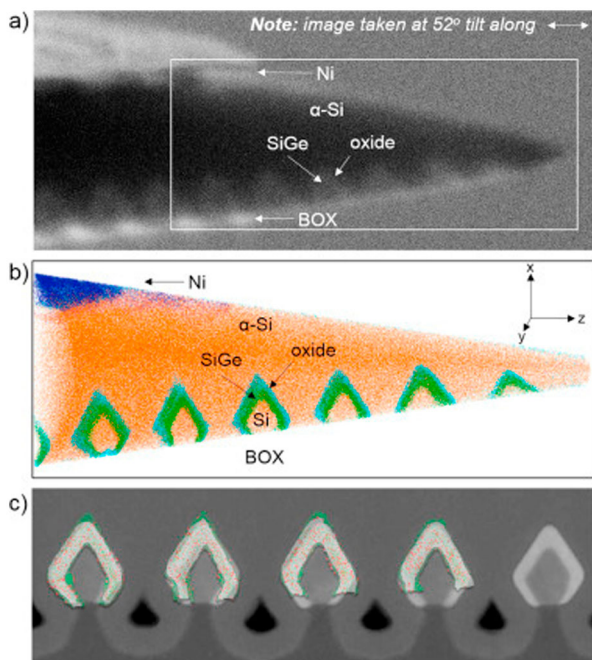


Figure 11. (a) SEM image of one of the tips prepared in this study with features indicated. (b) Reconstructed APT data from the tip shown in (a). (c) APT reconstruction with a Ge iso-concentration surface (green) and B atoms (red spheres) within the SiGe overlaid on a TEM image from a nearby location on the same wafer. Scale bars not shown for proprietary reasons (adapted from [86]).

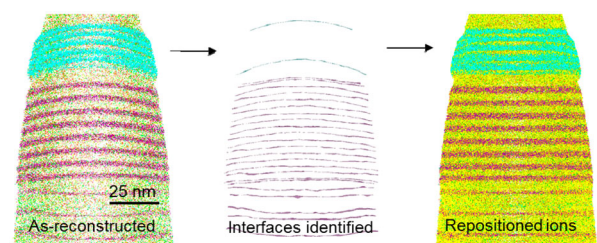


Figure 12. Example of a post-reconstruction correction approach (landmark reconstruction) utilising plane flatness as a metric for correcting ion positions. This GaN LED device structure includes layers of AlGaN and InGaN which are known to be flat and parallel to each other based on TEM measurements, yet there is no combination of reconstruction parameters which accurately reproduces these features throughout the entire dataset (adapted from [101] courtesy of Brian P. Geiser).

and weakness of the method. As we look into the future, there is certainly a call for alternative reconstruction approaches, particularly for the characterisation of electronic device features which can have complicated 3-D structures or features which are not well reproduced with the current method; however, alternate reconstruction algorithms almost certainly will be more complicated which will make broad-based adoption challenging.

Landmark Reconstruction is one example of an alternative reconstruction approach. Figure 12 shows the reconstruction of a multi-layer LED quantum-well device structure where each layer is known to be flat and parallel to its neighbours. It is not possible to choose a single set of point-projection-reconstruction parameters that provides accurate reconstruction for the entire analysis volume. Here, a post-reconstruction correction approach is used to reposition atoms and improve layer positioning accuracy. Selected chemical interfaces are flattened and these motions are propagated, orthogonal to the interface surface, to reposition atoms throughout the entire depth of the reconstruction (similar to [87,104]). Other enhancements or alternative approaches, such as variable reconstruction parameter approaches [105], integration of correlative measurements [106,107], and simulation-assisted reconstruction [96,108], have been reported and their progress is worth monitoring for improving reconstruction accuracy in difficult-to-reconstruct systems.

Correlative APT

Another method which can assist with the refinement of APT reconstructions and the extracted data is the use of correlative techniques. Here we define *correlative APT* to mean the combination of APT with other microscopy techniques, such as SEM, TEM, or STEM imaging possibly along with selected area, nanobeam, or convergent beam diffraction or electron backscattered diffraction (EBSD). In this case, correlative APT only refers to such multimodal imaging analyses where the imaging is conducted on the same needle specimen.

There are several important, often related motivations for correlative APT analyses. The most basic use of correlative work is for verifying that a specific region is contained within an APT specimen. This was the motivation behind the first implementations using TEM imaging of FIM specimens. More recently, a further goal is to realise a level of understanding beyond what can be achieved by the stand-alone APT analysis. Often atomic-scale structure, composition, and chemical state information are all desired for facilitating a comprehensive understanding of materials' properties. APT provides high-resolution compositional information, but generally requires correlation

with other microscopy and spectroscopy techniques to provide structural and chemical state information.

An additional motivation for correlative microscopy is to improve the accuracy of APT reconstructions. The additional information provided by correlative imaging techniques, such as specimen shape, locations, and orientations of features, tip tangential discontinuity, and depth removed offer constraints on the possible reconstruction parameter values and a means of assessing the accuracy of the reconstruction. While APT is a powerful 3-D nanoscale characterisation technique, there are a number of aberrations that arise due to the inherent physics of the field evaporation process that may result in an inaccurate reconstruction of the final APT data. Trajectory aberration, while analysing heterogeneous specimens, is one such aberration that is very important to understand when interpreting APT results from complex heterogeneous materials. To understand these aberrations and overcome this limitation, directly correlating APT with TEM is important.

As suggested in the preceding paragraph, correlative methods also provide a window into field evaporation effects, laser-material interactions, and the APT technique itself, which can further knowledge of the not-always-intuitive physical phenomena that occur at the nanoscale under high vacuum, at cryogenic temperatures, while subject to very high fields, and ultrafast laser pulses. TEM images of APT specimens both before APT analysis and after interrupted APT analysis have already been shown to provide important information which can be utilised to understand the physics of field evaporation and improve the accuracy of APT reconstructions [109]. Further advances in these areas might lead to improvements in both current instrument and reconstruction limitations of APT especially for complex heterogeneous materials.

The earliest efforts in correlative atom probe and TEM were performed in the 1960s [34,35]. These used TEM to target grain boundaries in electropolished wire specimens for subsequent field ion microscopy (FIM) analysis. Over the next several decades, only a few similar types of correlative analyses were published [36,37,110]. The advent of the commercial LEAP along with FIB instruments for specimen preparation produced renewed interest and new possibilities for correlative work. In one of the early efforts directed specifically towards correlative LEAP-TEM analyses, Gorman *et al* designed a correlative APT-TEM holder that facilitated the transfer of a 1-D array of APT specimens prepared on a TEM half grid between FIB, TEM, and APT instruments [39,49]. Similar 1-D arrays geared towards the specifics of other microscopes have subsequently been developed [41,42,102].

Among the first demonstrations of directly correlating STEM with APT was STEM tomography and APT

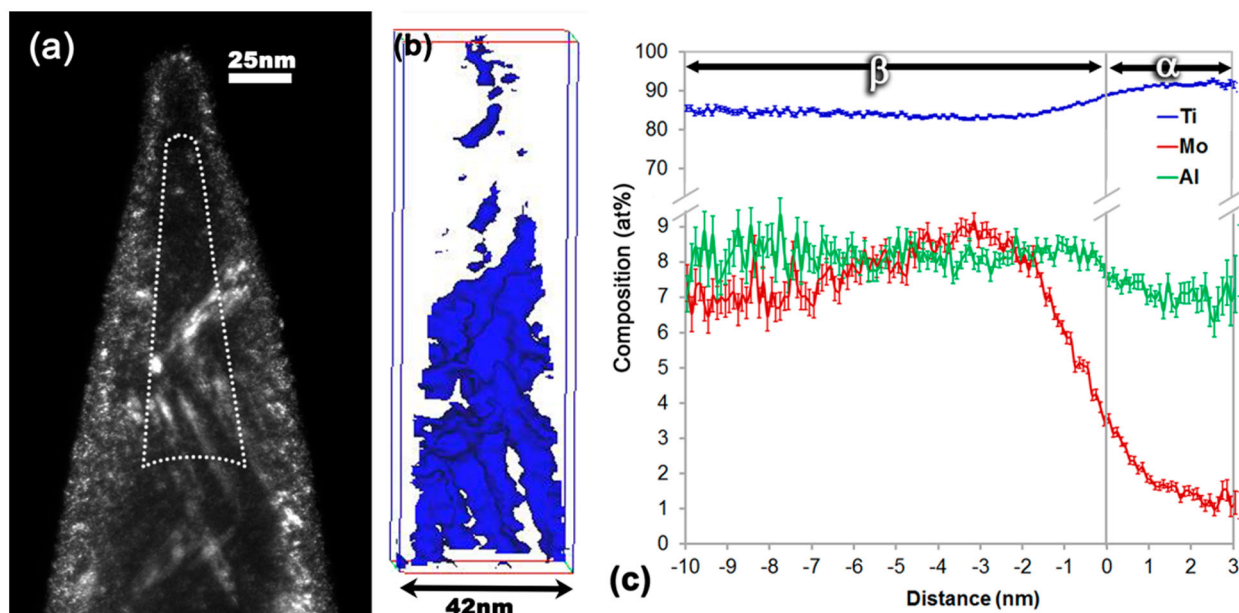


Figure 13. An example of direct correlation of APT with TEM aiding in accurate identification of precipitate regions within the APT reconstruction of the multicomponent beta Ti alloy: (a) Dark field image of an APT needle specimen of a Ti–Al–Mo alloy; (b) Ti 93 at.% isoconcentration surface of the APT result highlighting the alpha-phase precipitate region; (c) proximity histogram showing the solute partitioning between the alpha and beta phases (adapted from A. Devaraj *et al.*) [112].

of Ag-rich GP zones in an Al matrix by Arslan *et al.* [38]. The comparison allowed direct visualisation of theoretically known reconstruction artefacts present in both electron tomography and APT and, therefore, better overall assessment of particle morphology and composition than available through either technique alone. The first examples of direct correlation of APT with aberration-corrected TEM [111] and aberration-corrected STEM [109] were also published recently. There are several examples of using APT–TEM correlation for a variety of materials: metals and alloys, [112–115] bulk metallic glasses, [102] NWs, [49] bulk oxides, [111,116] oxidation of metals, [117,118] metal-dielectric composites, [109], and semiconductor heterostructures [119]. More recently, there have been some notable efforts in conducting direct correlation of EBSD in an SEM or precision nanobeam diffraction in a TEM with APT, [120] which provide detailed crystallographic information of materials, such as misorientation angles of grain boundaries, which are critical for developing statistically significant measures of grain boundary segregation in materials [42,120,121]. An example of correlative APT is shown in Figure 13, where dark field imaging of an APT specimen of a Ti–Al–Mo alloy shows a cluster of alpha-phase precipitates distributed in the beta phase before APT. This is compared with the isocomposition surface view of high Ti concentration and the corresponding proximity histogram; this combination helps quantify the solute partitioning across the alpha and beta phases. Without the TEM dark field image of the needle specimen, it would have been difficult to conclusively identify the alpha-phase region compositionally from the

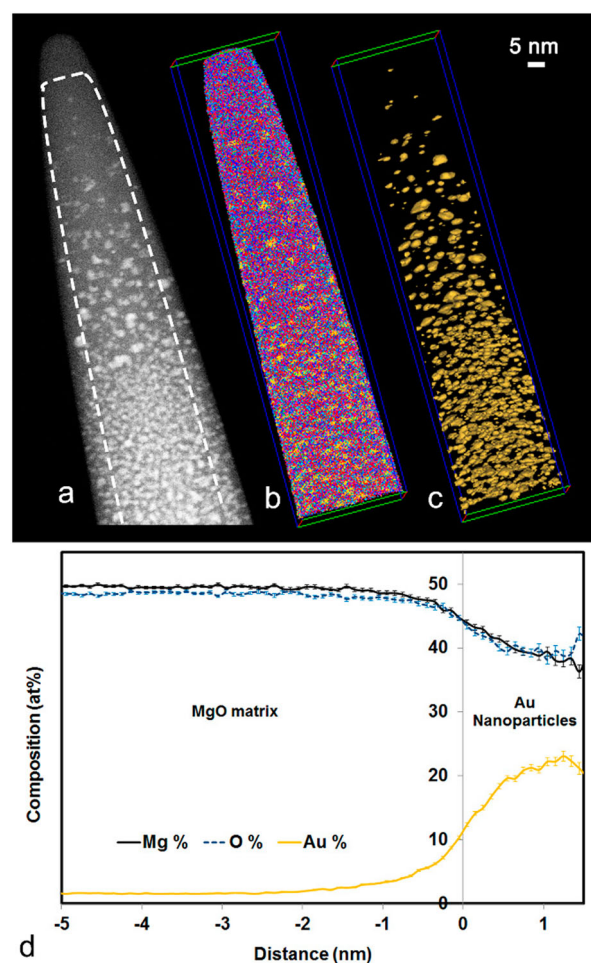


Figure 14. Aberration-corrected STEM–APT direct coupling for Au nanoparticles embedded in MgO along with the proximity histogram showing the composition change across the Au nanoparticles and MgO matrix [109]. (Image courtesy A. Devaraj, PNNL).

multi-element APT result alone [112]. An example of correlative APT-aberration-corrected STEM imaging is provided in Figure 14; Figure 14 (a) shows the STEM image of Au nanoparticles embedded in an MgO substrate, (b) and (c) show the APT results with Au nanoparticle regions highlighted in yellow and (d) show the composition partitioning across Au nanoparticles and MgO matrix in Au–MgO.

Applications of APT in materials analysis

Atom probe analysis of metals and alloys

From the time of 1-D atom probes, early applications of APT were predominantly dedicated to microstructural characterisation of metals and alloys. Extensive literature is available on the application of APT analysis towards understanding a variety of phase transformation phenomena in metals and alloys. While this review is not a comprehensive coverage of the vast literature, some key examples are provided to highlight the unique capabilities of APT as a nanoscale analytical tool for metals and alloys.

Over the last few decades, APT has become a critical characterisation capability that provides unique compositional, and in some cases structural, information of metallic alloys at subnanometre scale spatial resolution. These have been shown to correlate well with atomistic and continuum scale material models and simulations [122]. Within the broad class of phase transformations, we have specifically focused on providing examples of utilisation of APT for understanding different types of solid-state phase transformations in metals and alloys. Providing a complete list, even within this class of phase transformations, is nearly impossible because of the current widespread use of APT. Here we present a few examples that, in our opinion, represent unique contributions from APT towards understanding phase transformations in metallic alloys.

APT is especially useful for understanding the compositional partitioning between phases in diffusional solid–solid phase transformations in metallic alloys. The diffusional phase transformations correspond to those that occur due to thermally activated movement of atoms. Within the wide class of diffusional phase transformation, precipitate nucleation, and growth has been widely studied in many different metallic alloys using APT, where the data provides nanoscale compositional information of precipitates at various stages of the precipitation process. APT has been especially beneficial for understanding precipitation in many different classes of aluminium alloys (with a few hundred research publications from groups around the world), precipitation of second phases in titanium alloys [123–127] shape memory alloys [128], nickel-based superalloys [128–131], steels [132–134],

magnesium alloys etc. An example is provided in Figure 15, where APT was key in obtaining the composition of H-phase precipitate in a ternary Ni–Ti–Hf alloy [128]. This, in turn, was used in conjunction with electron diffraction and STEM imaging results to form a structural model for first-principles simulation-based energy minimisation studies [128]. Similarly, APT measurements of precipitate composition and interfacial segregation have been correlated successfully to results from CALPHAD calculations in steels [76,131–135] and Ni-based superalloys [129], first-principles calculations in steels [136,137] and Al alloys [138], and lattice kinetic Monte Carlo simulations in Ni-based superalloys [129].

One significant area of contribution of APT has been in analysing solute clustering in alloys which can be early stages of precipitation. Two extant core methodologies that have different fundamental basis, the maximum separation distance method [139,140] and the proximity histogram method [141–143], are often employed to delineate and characterise well-defined clusters in APT data, where the term cluster denotes a grouping of atoms. Thus, a cluster in context of APT data can either be a solid-state concentration fluctuation or a well-developed precipitate. Other methods, such as sampling by a region of interest (ROI), 1NN approach, Fourier transforms, and autocorrelation methods, are also used depending on the nature of the solute cluster to be analysed [144].

The maximum separation distance method relies on a recursive search algorithm for solute atoms based on the fact that the maximum separation distance, d_{\max} , between selected solute atoms is expected to be closer within a precipitate phase than in the matrix phase. A second user-defined parameter, N_{\min} , is also used for this method, which is the minimum number of solute atoms that a cluster should have to call it a cluster. All clusters identified with less than N_{\min} solute atoms are considered as a part of the matrix atoms. Variations to this method include the double maximum separation method with erosion [140] and the envelope methodology [145], which use additional parameters to delineate clusters from matrix atoms. The method is sensitive to the actual values of the two aforesaid parameters. The quantity d_{\max} depends on the lattice parameter, cluster composition, nominal concentration of solute atoms, and detection efficiency of the atom probe instrument. Vamousse, *et al.* suggested a broad range between 0.4 nm and 1.0 nm [140]. Kolli and Seidman [136] proposed a method whereby the total number of clusters of a selected solute atom is plotted as a function of the quantity d_{\max} . A local minimum on this plot indicates a reasonable value for the quantity d_{\max} that is great enough to not artificially split large clusters into smaller clusters, but also small enough not to incorrectly assign solute atoms from the matrix to clusters or incorrectly

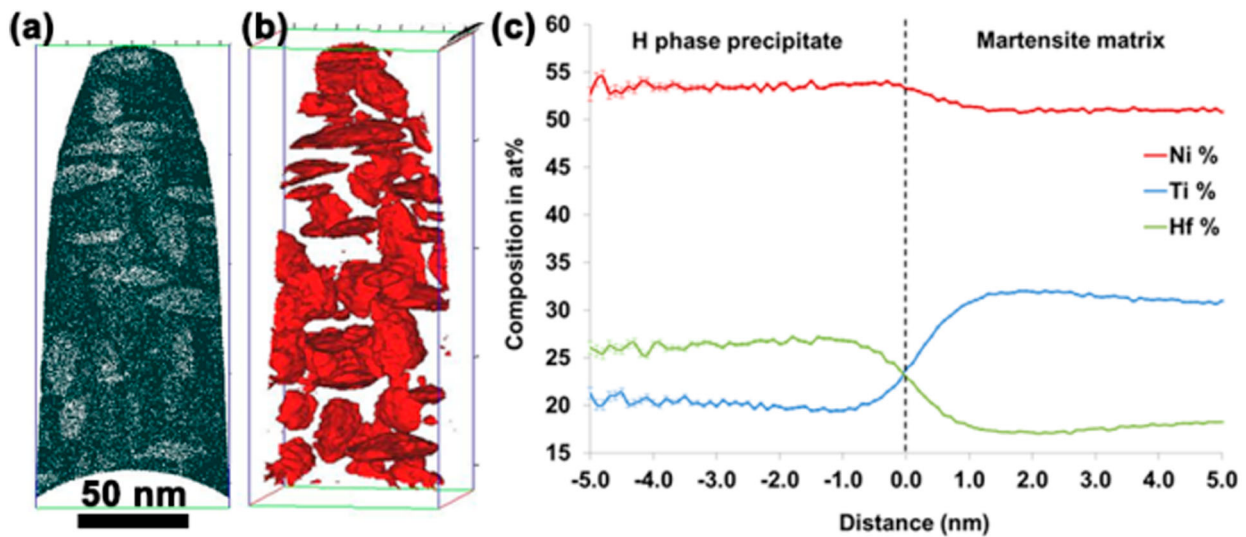


Figure 15. APT results from a Ni–Ti–Hf alloy showing (a) Ti depletion in H-phase precipitate regions in the Ti atom map (b) 23 at.-% Hf isocomposition surface highlighting the Hf-rich H-phase regions and (c) proximity histogram across the precipitate and matrix, which helps in quantifying the solute partitioning (adapted from Fan Yang *et al.*) [127].

combine adjacent clusters into a larger one. The authors suggested a value of d_{\max} between 0.5 nm and 0.7 nm to delineate Cu-rich precipitates in isothermally aged multicomponent Fe–Cu steels [136]. The value of N_{\min} is dependent on the choice of d_{\max} . Vaumousse, *et al.* [140] suggested a broad range of, between 10 and 30, atoms for the quantity N_{\min} . Kolli and Seidman [136] proposed that the quantity N_{\min} can be determined by plotting the distribution of clusters as a function of the number of atoms in a cluster for a given value of d_{\max} . A reasonable choice for the value of N_{\min} eliminates clusters that contain few atoms and gives a stable number of precipitates, i.e. changing N_{\min} does not significantly change the number of precipitates.

The isoconcentration surface method identifies precipitates or clusters using a concentration threshold, $c^{\text{threshold}}$, based on the fact that the concentration of solute atoms within a precipitate or cluster is greater than that in the matrix phase. A proximity histogram (proxigram for short) concentration profile, which is the weighted superposition of concentration profiles, is generated by binning atoms in fixed distance increments from the reference isoconcentration surface. This yields a 1-D concentration profile as a function of distance from the isoconcentration surface. By convention, positive distances from the interface are defined as the precipitate or cluster, whereas negative distances from the interface are defined as the matrix phase. The quantity $c^{\text{threshold}}$ must be chosen carefully to properly define the isoconcentration surfaces such that the selected value generates morphologically stable results. Small changes in the value of $c^{\text{threshold}}$ should not vary significantly the number of precipitates or clusters and their dimensions. If the value is too small, then the precipitates may be larger than their

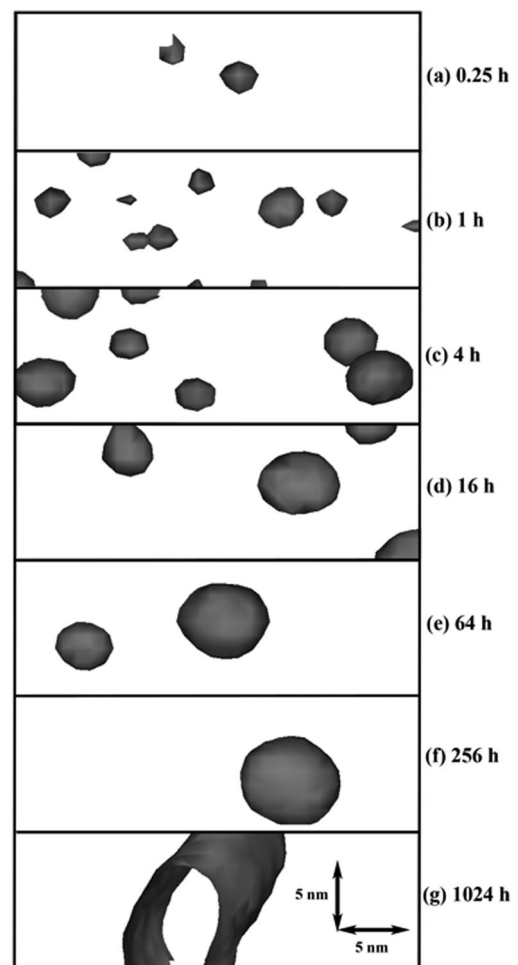


Figure 16. Copper-rich precipitates as delineated by 10 at.% Cu isoconcentration surfaces, when the steel is aged at 500°C for: (a) 0.25 h; (b) 1 h; (c) 4 h; (d) 16 h; (e) 64 h; (f) 256 h; (g) 1024 h. Each reconstruction, $10 \times 10 \times 30 \text{ nm}^3$ (3000 nm^3), is a subset of an analysed volume and contains approximately 130,000 atoms (adapted from [131]).

true size or smaller precipitates may be convoluted with nearby larger precipitates, and if too great a value is chosen, they may be smaller than their true size. The most widely used method that was developed by Hellman, *et al.* [141–143] relies on selecting a voxel size, delocalisation distance, and confidence sigma value. The voxel size is the three-dimensional (3-D) grid spacing in the concentration space. The delocalisation distance is chosen to spread the contribution of each atom to adjacent grid points, effectively smoothing the data and improving the statistical error. The confidence sigma value is chosen to give isoconcentration surfaces with a defined statistical uncertainty. By selecting a value for $c^{\text{threshold}}$, isoconcentration surfaces are generated thereby identifying the precipitates, Figure 16. Kolli and Seidman [136] applied both the envelope and isoconcentration surface methodologies in a multicomponent Fe–Cu steel. They carefully optimised the selection of parameters in both methods and demonstrated that the results were qualitatively similar. The concentration profiles created using both methods illustrated the presence of Cu-rich precipitates with elevated concentrations of Ni, Al, and Mn at the heterophase interfaces. The morphologies of the precipitates delineated by both methods were also compared and the number of identified precipitates varied by small quantities and there also existed differences in the measured radii. The quantitative variations are due to the technical differences in the basis of the two methods.

Within the broad area of precipitation in alloys, some of the metallic alloy systems undergo phase decompositions to form ordered precipitates that enable the retention of high temperature properties close to their melting temperatures. Since the ordered precipitates have well-defined chemical identity at sub-lattice positions, the occupancies of various alloying elements at these sub-lattices and their relative influences on each other govern the high temperature stability of these precipitates. APT has been proved to be an invaluable tool for accurate atomic-scale chemical and structural analysis of these ordered precipitates in Ni-base, Co-base superalloys, and Al alloys [146–150]. In some of the previous reports, the occasional atomic plane resolution in atom probe reconstructions has enabled structural analysis; such as determination of solute site occupancies in Ni-base superalloys. The reproducibility and versatility in characterising multiple crystallographic orientations from APT results was rather limited [151,152]. The advanced treatment of atom probe data to clearly observe various crystallographic poles in the ion desorption image and further identification of specific locations of crystallographic planes by utilising protocol like Fourier transforms and Hough transforms have improved the structural analysis significantly [70,71,153]. The standard algorithm used for structural

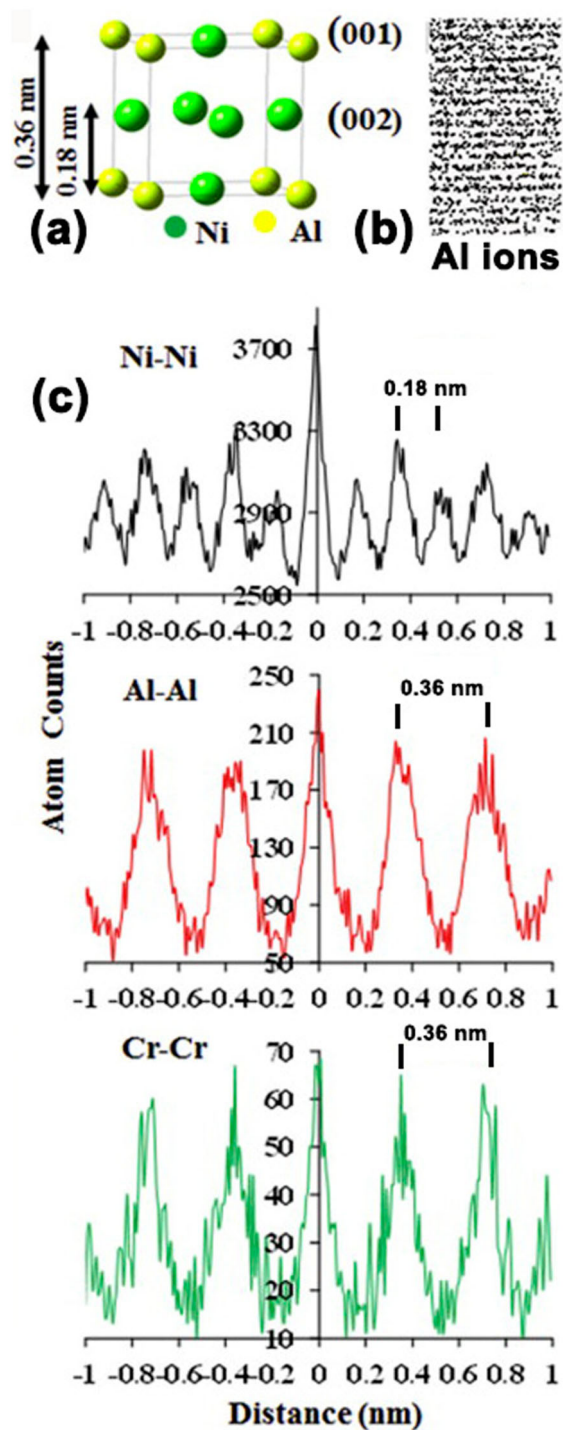


Figure 17. Ordering and site occupancy in Ni_3Al revealed by z spatial distribution maps (adapted from Meher *et al.*) [157].

analysis, SDM, is basically a combination of two individual radial distribution functions, one of which has a species-specific 1-D nature along the analysis axis (z -SDM) [71]. This modern treatment of atom probe data for structural analysis has led to a new field, atom probe crystallography, which has proved successful in 3-D orientation mapping of grain boundaries in nano-crystalline materials and determination of atomic plane orientations in pure metals or dilute alloys [154–156]. But, its application to multi-components systems involving solute elements with high

evaporation fields seems improbable because of the reduced visibility of crystallographic poles in the ion desorption map.

Recently, Meher *et al.* developed a method for crystallographic study that overcomes the tedious mathematical treatment of atom probe data and is also applicable to various highly alloyed systems [157]. In this reproducible approach, the precise site-specific sample preparation with the help of EBSD retains the crystallographic information in spite of poor visibility of poles in ion desorption image. This method has enabled the determination of solute site occupancies in highly alloyed Ni-, and Co-base superalloys [158,159].

This method of coupling of orientation microscopy with APT has immense potential for extracting atomic-scale information in a variety of materials. As an example, Figure 17 shows the determination of solute site occupancies in ordered Ni_3Al precipitates in a ternary Ni-14 Al- 7 Cr at.% alloy where the samples were prepared from a $\langle 001 \rangle$ oriented grain, identified by a conventional EBSD method in a FIB [157]. Figure 17(a) shows a schematic of specific atomic arrangement in a basic Ni_3Al precipitate, while Figure 17(b) shows (001) lattice planes specific to Al ions obtained only by APT. The 1-D z-SDM specific to each element, as shown in Figure 17(c), is a clear representation of a depth resolution better than an inter-atomic spacing along the analysis axis in APT. The SDMs clearly resolve the presence of Ni atoms in every (002) plane, separated by a distance of 0.18 nm, while Al and Cr were observed to be separated by a spacing of 0.36 nm indicating locations on (001) planes. Thus, it appears that Cr atoms have the tendency to substitute for only Al atoms in the Ni_3Al , and hence, modify the chemical formula to $\text{Ni}_3(\text{Al,Cr})$ [158].

Another kind of solid–solid phase transformation that has been studied using APT is eutectoid transformation. During eutectoid transformations, a single-phase transforms to a mixture of two different phases. One classic eutectoid transformation is the formation of pearlite in steel. APT can provide unique

insights into the atomic-scale mechanisms of eutectoid transformation, especially by providing an accurate estimation of solute partitioning at interfaces across the lamellar phases [160–164].

Another significant and unique contribution of APT has been for aiding in compositional quantification of phase separation in alloys by spinodal decomposition [165–167]. APT can provide quantitative information on the amplitude and wavelength of the compositional modulations as a function of time in alloy systems prone to spinodal decomposition [168–172]. For example, APT has been used extensively to study the correlation of microstructure resulting from spinodal decomposition with various mechanical and magnetic properties of Fe–Cr-based alloys [173]. Another example of use of APT in studying spinodal decomposition in Ti alloys is provided in Figure 18, where a combination of aberration-corrected STEM imaging and APT is used with first-principles density functional theory (DFT) nudge elastic band (NEB) calculations for estimating energy barriers for the beta to omega phase transformation in a Ti–9 at.% Mo alloy. In the aberration-corrected STEM image (Figure 18(a)), the presence of bright and dark regions within a quenched microstructure was observed with a displacive transformation within the darker pockets. Based on APT results, particularly the proximity histogram given in Figure 18(b), Mo partitioning was observed that could be directly attributed to the observed contrast in STEM images. Then using DFT–NEB calculations, a composition-dependent change in the energetics of the phase transformation was identified (Figure 18(c)). These results indicated the existence of a new mechanism of phase transformation with a combined diffusive–displacive component [122].

Another significant contribution of APT has been in understanding crystallisation of amorphous metallic materials like bulk metallic glass or immiscible metal alloy systems [174–179]. Immiscible alloys, when subjected to heat treatments, can lead to devitrification to form nanocrystal precipitates in an amorphous matrix during the initial stage of annealing followed by a

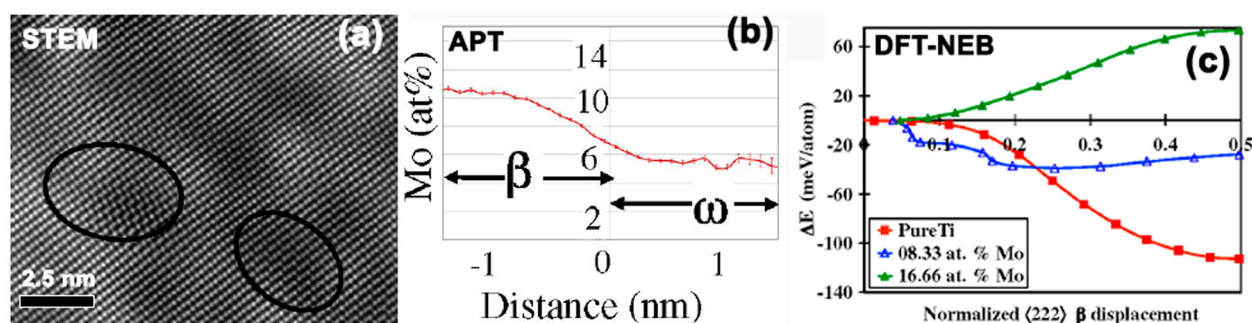


Figure 18. (a) Filtered high angle annular dark field–high resolution STEM image of Ti–9 at.% Mo along a $\langle 011 \rangle$ beta zone axis, with black circles highlighting the dark contrast regions with partial displacive transformation; (b) proximity histogram plotted across a 93 at.% Ti isoconcentration surface showing regions of Mo enrichment and depletion; (c) NEB calculation for the energetics of the beta to omega phase transformation for 0, 8.33, and 16.66 at.% Mo alloys [122] (adapted from S. Nag *et al.*) [122].

complete crystallisation. APT can aid in accurate quantification of the compositional partitioning between the crystalline phase and amorphous matrix and help validate mass balance models for solute partitioning as highlighted by DeGeorge *et al.* for APT analysis of amorphous $(\text{Fe}_{65}\text{Co}_{65})_{79.5}\text{B}_{13}\text{Si}_2\text{Nb}_4\text{Cu}_{1.5}$ nanocomposites [176].

APT has also been essential for investigating solute segregation to material defects like dislocations or grain boundaries in alloys [113,180–184]. Through many publications by M. K. Miller, the capabilities of APT in quantitatively measuring solute segregation to dislocations and imaging the formation of solute clusters and second phase precipitates along dislocations have been demonstrated for multiple nuclear structural steels [180,185].

Gaining quantitative measurements of segregation of elements at grain boundaries in alloys either as a function of different heat treatments or neutron irradiation has also been a notable application of APT. Site-specific sample preparation using FIB in conjunction with either EBSD in SEM or nanobeam electron diffraction in TEM has permitted very precise targeting of grain boundaries in alloys for APT analysis [42,120,186,187]. More recently, by utilising the developments in deciphering crystallographic information from the crystallographic poles observed in APT results, Moody *et al.* have also demonstrated the characterisation of grain boundary misorientation from APT results of nanocrystalline aluminium [155].

Atomic-scale dopant distribution in semiconductor devices

The advent of laser-assisted APT has made it possible to probe the structure of semiconductors at a level never seen before. The combination of nanoscale resolution (~ 0.2 nm) and chemical composition provides a unique place for APT in the semiconductor industry where individual devices and layers can be probed. The device properties and performance are directly influenced by the dopant levels, carrier concentrations, impurities, and defects present in the system. Thus, a thorough study of all the aforementioned parameters is necessary to understand their effects on device performance.

Initial reports on laser-assisted APT of semiconductors dealt with Si, alumina, and SiC as well as III–V semiconductors, such as InAs and InP [188]. The ability to study dopant profiles, impurities, and defects at low concentrations of $< 1 \times 10^{18} \text{ cm}^{-3}$ using APT enabled extensive studies of Si semiconductors. One of the early APT studies of Si–Ge epitaxial layers, relevant to the performance of bipolar transistors and metal–oxide–semiconductor field effect transistor (MOSFET) devices, revealed abrupt interfaces measuring 2–3 nm between Si and Ge [189].

Thereafter, Thomson *et al.* imaged the Cottrell atmospheres in As implanted Si by both TEM and APT and observation of As defects was then related to structural integrity and device performance [190]. APT has also been used to study shallow and deep implants in Si. Shallow implants occur in active regions of the transistor at the source and drain, and are usually high in concentration (1%–2%). Deep implants refer to implants over tens of nanometres. Ronsheim *et al.* studied As and B dopant locations and concentrations in Si using dynamic secondary ion mass spectrometry (SIMS) and laser-assisted APT [191]. Their study focused on shallow dopant profiles in planar devices, indicating the accumulation of As under the gate oxide layer which appeared to increase on further annealing at 1000°C for 30 seconds.

Apart from dopant distribution, nickel silicide contacts have also been investigated [192]. The low resistivity of nickel silicide, its low temperature of formation and its lower Si consumption allowed adoption by the industry. The main drawbacks of the Ni system were (1) increase in resistivity due to agglomeration of the NiSi (desired) phase, and (2) formation of the higher resistivity NiSi_2 phase during silicide processing. The addition of transition metals, such as Pd, Pt, or Rh, was shown to prevent NiSi_2 phase by an increase in formation temperature as well as a reduction in agglomeration of the NiSi phase. Using APT, Kim *et al.* [193] explained this phenomenon. Driven by a decrease in the interfacial Gibbs free energy, Pd segregated at the NiSi–Si interface. This decreased the driving force needed to agglomerate NiSi_2 , and a stable NiSi film that was resistant to morphological degradation was formed.

APT was also used to measure the thickness and uniformity of gate dielectric stacks and dielectrics with high dielectric constant κ . Larson *et al.* [194] probed 20 nm thick films of SiO_2 and Al_2O_3 . Their results identified the SiO_2 composition to be slightly oxygen deficient and the Al_2O_3 composition to be slightly oxygen enriched. Ulfing *et al.* [195] studied the composition of light elements in ALD deposited hafnium-based high- κ dielectrics using APT. The compositional integrity of hafnium-based high- κ films, deposited through two distinct surface preparation techniques, was analysed. The study confirmed that a non-uniform dielectric film was formed when the native oxide of Si was removed with hydrofluoric acid (HF) prior to deposition of the high- κ dielectric film.

Although not a comprehensive list, the studies until 2009 discussed so far indicated the viability of APT for the field of semiconductor devices. Till 2009, all studies were limited to thin films, interfaces and bulk doping profiles and analysis of entire devices was lacking. Subsequently, Inoue *et al.* reported on laser assisted APT of

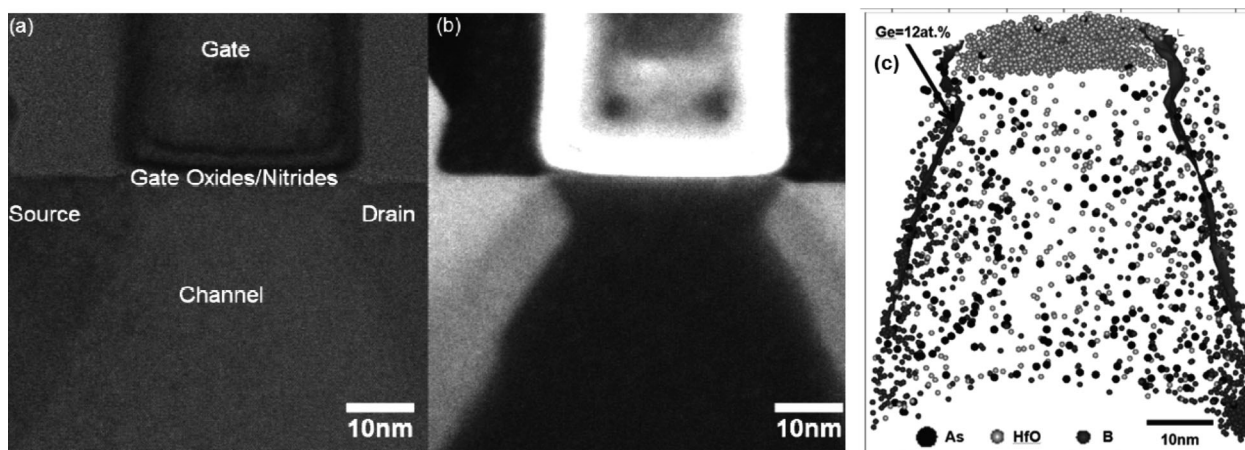


Figure 19. (a) Bright field (b) high angle annular dark field STEM image and (c) APT result of Intel i5-650 device [196].

n-type MOSFET devices [196]. The distribution of As, P, and B dopants across the source/drain and gate regions was identified. P doping in the gate region and As doping in the source/drain region was also observed and a clear SiO_2 gate oxide layer was also imaged using a LEAP 3000X HR APT system. Their report provided the proof of concept to allow the foray of APT into the semiconductor industry as an integral technique to study transistor device compositions. Another effort by Larson *et al.* characterised the source, drain, channel regions, and gate oxide of a commercial Intel i5-650 p-FET by both APT and STEM imaging (Figure 19) [197]. As an analysis tool, the power of APT lies in its ability to investigate each successive generation of transistor devices even as the scale continues to diminish. Moreover, the 2-D projection and averaging of information obtained from TEM is no longer a hindrance for APT, which is truly a 3-D technique.

With the introduction of FinFETs – 3-D field effect transistors with a wraparound fin – the suitability of APT could not be more aptly described. The transition from planar to 3-D device architectures required new metrology approaches to characterise the 3-D dopant and carrier distributions more precisely, as their positioning relative to gate edges, 3-D distribution, conformality, and concentration would determine the device performance in its entirety [197].

Over the years, a multitude of reports have been published on using APT to study FinFET dopant distributions. Kambham *et al.* [198] reported on B dopant distribution using ion implantation at two different tilt conditions, (45° and 10°). They observed a uniform dopant distribution for a tilt angle of 45° , but there was a clear B sidewall distribution for 10° . Furthermore, the effect of Ga implantation during the annular milling process was also investigated. Takamizawa *et al.* [199] were the next to report on B doping in FinFETs, but they achieved the doping using self-regulatory plasma doping (SRPD). They were able to study different sections of the fin as well as study the fins at

different angles to investigate the gate oxide thickness and boron conformality.

More recently in 2015, Han *et al.* [200] reported on the P and B diffusion pathways in polysilicon gates using APT. Based on the annealing times, in the initial stages of diffusion, P diffused deeper along the grain boundaries, away from the implanted region. As the annealing time was increased, the P was found to be segregated on the grain boundaries. However, with B, the trend was reversed, with segregation observed only during the initial stages of diffusion followed by a uniform doping.

Although laser-assisted APT had been used to study dopants and carrier concentrations in 3-D FinFET devices, one important aspect was still missing. All previous studies lacked site specificity. A random trench or fin was chosen for these studies, and the ability to investigate the characteristics of a transistor or fin of interest was still not demonstrated. Kambham *et al.* [201,202] reported on site specificity (~ 50 nm in each dimension) achieved via ion beam-induced deposition of a cylindrical Pt feature on top of the ROI. The location of the fin was identified using the topography of the pad oxide. Issues regarding the size and exact location of the identification mark were also discussed, with possible ways to mitigate them. For this study, a fin height of 60 nm, fin width of 40 nm, and a gate width of 50 nm were used. Their study identified a clear underdiffusion of As dopant from the source/drain to gate region and a non-conformality in the As dopant distribution under the fin. In another report by Kambham *et al.*, [203] they simulated the SRPD process and performed a statistical analysis comparing the experimental atom probe and simulation results, based on which As clustering was identified as the primary mechanism for dopant deactivation.

The devices, under investigation by Kambham *et al.* though landmark to the field, did not involve as-fabricated chipsets or memory devices. In early 2013, Panciera *et al.* [204] reported on APT of static random access memory transistors smaller than 30 nm

consisting of Ni silicide contacts, metal gates, and high- κ dielectrics. For the analysis, atom probe tips were fabricated using the top-down and backside approach. The backside approach allowed easier fabrication, but was not preferred due to the increased chances of tip fracture and degradation in mass resolution. Issues with tip fracture due to the presence of W were also identified and mitigated by chemically etching W and using FIB-deposited Pt plugs. In their work, high-resolution SEM imaging was used to identify polysilicon gates to achieve site specificity followed by the rotation of the FIB stage by $\pm 90^\circ$ between each milling step for improved precision. Their atom probe results clearly showed the silicide contacts, polysilicon gates, and TiN capping. In the same year, Hatzistergos *et al.* [205] from IBM reported on APT of 14 nm FinFET devices, albeit without any site specificity. They reasoned that the small size of the transistor, which followed a repeated array in two dimensions, would ensure that any tip contained at least one transistor.

As previous reports show, APT presents a significant advancement in the analysis of semiconducting devices, but being a relatively new technique, the field still needs development in both sample preparation and analysis. Reconstruction issues and differing evaporation fields for heterojunctions need to be accounted for to ensure more precise and accurate determination of the various layers in FinFETs. Grenier *et al.* [206] showed the deviation in morphology of Si NW gate-all-around (GAA) devices due to the local magnification effect. Differences in the evaporation fields of Si and the surrounding oxide layers cause the ion trajectories to be focused, leading to a compression in the lateral dimensions of the Si NWs. Using complementary data from electron tomography, they were able to correctly analyse the dimensions and composition of the Si NW and gate oxide layers. Gilbert *et al.* [207] also observed a similar distortion of the Si fin structures with high- κ dielectrics. Koelling *et al.* [208] also reported similar compression in SiGe layers using both FIM and APT. Differences in penetration depth of different lasers (green and UV) were also responsible for the distortions observed. On the theoretical aspects, Silaeva *et al.* [209] studied the physics and chemistry of field evaporation for semiconductors. They discussed electric field characteristics on the microscopic and macroscopic level as well as the kinetics of field evaporation.

The most pressing issue, though, relates to the evolution of the tip shape instantaneously during the experiment, which deviates from the hemispherical shape assumed in reconstruction algorithms. To address this, Vurpillot *et al.* suggested an improved reconstruction algorithm that takes into account complex geometries and flat interfaces [94].

All these studies demonstrate the prowess of laser-assisted APT in effectively identifying dopant profiles

related to various implantation schemes. Analyses of semiconducting devices have revealed the 3-D structure of source, drain, gate, and gate oxide layers at the nanoscale. The future for the semiconductor industry and researchers at large is to be able to push the limits in the analysis of each successive generation of electronic devices. As the devices get smaller, the ability to achieve site specificity within 10–15 nm presents a significant challenge. As an analysis tool, the unique functionality of APT will allow its widespread adoption for routine analysis of new generations of semiconducting electronic devices. Further improvements in the reconstruction algorithms and challenges involving site specificity during sample preparation within 10–15 nm would be the next benchmark for this technique.

Atomic-scale compositional mapping of semiconductor nanowires

Semiconductor NWs are a class of low-dimensional nanomaterials that have received considerable attention since the early 1990s for application in electronic, magnetic, optical, sensing, and power generation and storage devices. As with bulk and thin film semiconductor materials, the properties of interest for NWs are largely determined by composition and morphology, specifically the presence of impurities and/or the morphology of buried interfaces. The rational engineering of NWs with desired properties for advanced applications thus relies on a feedback loop between knowledge of the composition, morphology at the atomic level, and the scheme used to synthesise the NWs. The identification of impurities in NWs has important implications for the understanding of both the growth process and the electronic transport characteristics. APT is an analytical technique that is currently being applied to NWs to determine the composition with part-per-million sensitivity and the distribution of individual atoms with atomic-scale resolution.

In this section, we review the APT analysis of semiconductor NWs to cover some important accomplishments; it is not meant to be an exhaustive review of all related reports. Key examples are provided of analyses revealing the distribution of both intentional and unintentional impurities, as well as buried interfaces, as no other technique today can.

The incorporation of intentional impurities, known as dopants, is fundamental to controlling the electrical properties of semiconductor NWs by the modulation of the carrier type. The first report of mapping the intentional dopant distribution and reporting concentration within NWs by APT analysis was made by Perea *et al.* for a doped Ge and Si–SiGe NW axial surrounded by a radial Ge shell [47]. In Figure 20(a), the distribution of individual B atoms is shown within a Si section that is surrounded by a Ge shell, while in Figure 20(b), the

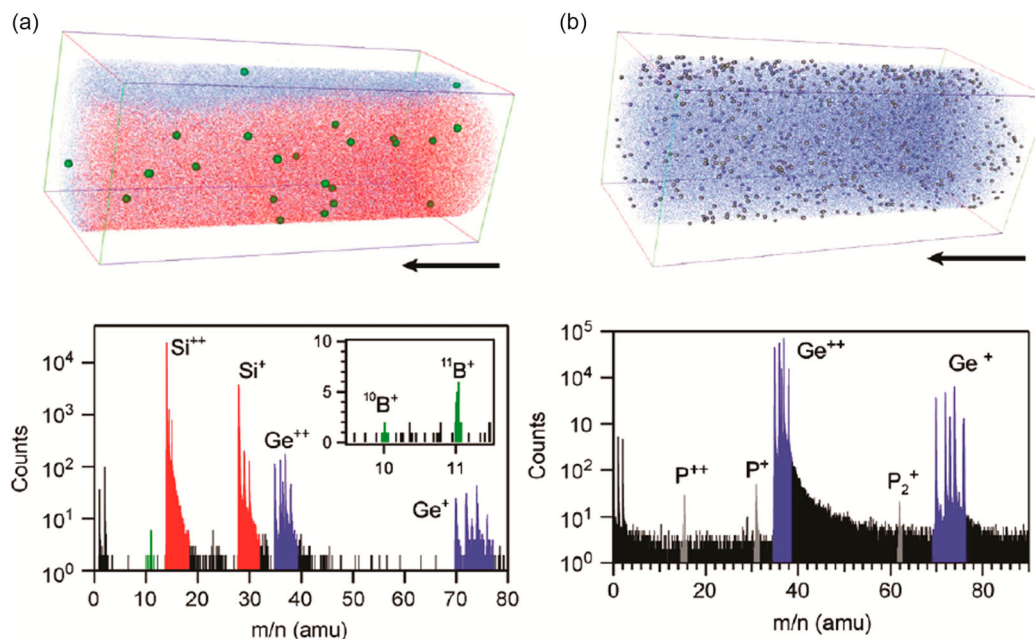


Figure 20. Mapping of intentional dopants. (a) 3-D reconstruction and associated mass spectra of a portion of a B-doped Si NW with an i-Ge shell; red = Si, blue = Ge, green = B. Reconstruction dimensions = $23 \times 23 \times 45 \text{ nm}^3$. (b) 3-D reconstruction and associated mass spectra of a portion of a P-doped Ge NW; blue = Ge, grey = P. Reconstruction dimensions = $45 \times 45 \times 75 \text{ nm}^3$. Both (a) and (b) are adapted from Perea *et al.* [47].

distribution of P atoms is shown within a Ge NW. The respective mass spectra are also shown, demonstrating the detection of dopant atoms as revealed by a distinct mass spectral signature above the background. By integrating the dopant and semiconductor counts and subtracting the background counts, the relative dopant concentration can be determined, which is commonly reported as a dopant density (number of dopant atoms/ cm^3 of semiconductor material). For example, in Figure 20(a and b), a B and P doping density of $1.1 \pm 0.2 \times 10^{19} \text{ cm}^{-3}$ and $1.0 \pm 0.2 \times 10^{18} \text{ cm}^{-3}$ were reported in Si and Ge, respectively [47]. The distribution of intentional dopants in other semiconductor systems has also been reported, such as N dopant atoms in ZnO NWs, [53] Si dopant atoms in GaAs NWs [210] and Mg dopant atoms in a GaN NW, [211] exemplifying the breadth of materials.

The contribution of unintentional impurities is also important when considering the electronic properties of NWs [212]. A potential extrinsic source of unintentional doping is background gases in the reactor, such as oxygen and carbon, that have the potential to become incorporated during synthesis. For example, Du *et al.* have reported the detection of C, H, and O in the APT analysis of GaAs NWs [210]. However, radial composition profiles show that the distribution of these unintentional impurities is localised at the surface and is likely a result of surface contamination during post-growth exposure to the atmosphere, with no clear signature within the NW interior.

For VLS-grown NWs, the unintentional incorporation of catalyst atoms can also occur, which can either have a deleterious effect on the transport properties,

such as Au in Si, or even contribute in a positive way to the doping of a particular type, such as p-type Al dopants in Si or Ge. This has been the subject of several studies that have confirmed the incorporation of dopant atoms. For example, the unintentional incorporation of catalyst atoms in varying semiconductor systems has been reported, such as Au in InAs, [45] Al in Si [213,214], and In in Si [215]. Although APT has a sensitivity to detect dopant densities $>10^{18} \text{ cm}^{-3}$, quantifying dopant levels less than this is a challenge due to an insufficient signal above the background. In such a case, an analysis of an *upper bound* to the number of dopants can be reported based on the background counts and associated statistical uncertainty in the spectral regions of interest [47,216].

Although APT can be used to map the relative concentration and distribution of dopants, inadequacies in detector spatial resolution and efficiency as well as unresolved aberrations in data reconstructions are preventing the analysis of dopant electrical activity. Instead, researchers are applying a multimodal approach to combine APT with other analyses that can assess dopant electrical activity and the nature of carrier conduction in NW systems. For example, correlative APT and electrical transport measurements have revealed how distinct dopant concentrations and distributions can influence the behaviour of devices [53,212,215,217]. APT-measured dopant concentrations and distributions are also being used to directly inform technology-computer-aided-design electronic transport simulations to probe the relative roles of interface states on carrier injection and extraction [218]. Additionally, the future combination of APT

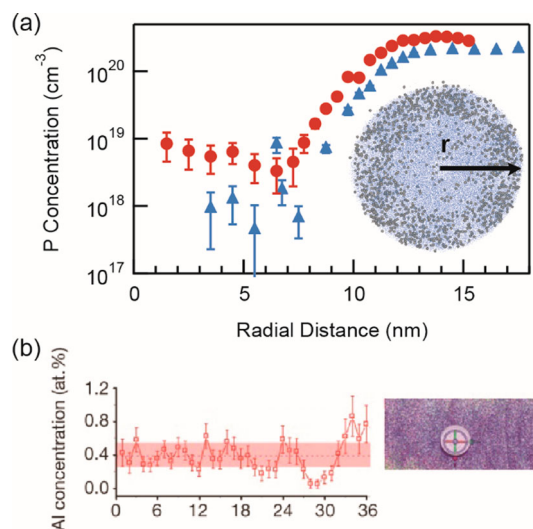


Figure 21. Quantification of radial dopant distributions. a) Radial concentration of P dopant atoms within a Ge NWs grown at 380°C and PH₃:GeH₄ ratios of 1:1000 (triangles) and 1:500 (circles). Inset shows an end-on view of the reconstruction with P as grey spheres and Ge as blue dots and the path along which the concentration was measured. Adapted from Perea *et al.* [221]. (b) Axial Al atom concentration profile in Si NW (left) measured within 8 nm diameter cylindrical segment (right). The horizontal dashed line denotes the average concentration of 0.39 ± 0.14 at.%; The shaded band is the uncertainty interval; Error bars represent ± 1 standard deviation. Adapted from Moutanabbir *et al.* [214].

and electron holography [219] and/or Kelvin probe microscopy will surely provide insight into active dopant incorporation efficiency.

The unique radial and axial tomographic mapping of impurities is important not only to help understand the resultant electronic transport characteristics in NW devices, but also to help develop a fundamental understanding of solute incorporation via the VLS mechanism [214,220,221]. In Figure 21(a), the quantitative radial distribution of P atoms in a Ge NW is shown by Perea *et al.*, [221] revealing the dramatic difference in P dopant atom incorporation through the liquid catalyst into the NW core versus incorporation via surface deposition, leading to a core-shell-like dopant distribution. In a similar analysis, Moutanabbir *et al.* analysed the Al atom distribution in Si NWs resulting from incorporation from a VLS-grown NW using an Al catalyst [214]. They found relatively constant axial and radial distributions of Al atoms without any Al clustering. In these reports, models connecting solute incorporation kinetics to the solution thermodynamics for the respective systems are presented that were directly informed by quantitative dopant profiles.

Battery materials

In the context of energy storage materials, so far there are only a few demonstrations of successful application

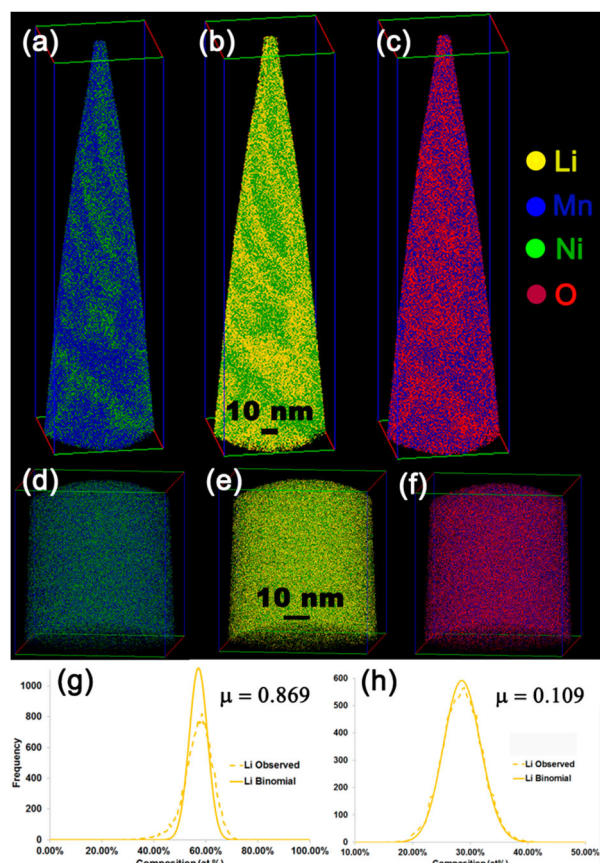


Figure 22. APT results from two advanced Li-ion battery cathodes (a–c) showing elemental maps of layered Li_{1.2}Ni_{0.2}Mn_{0.6}O₂ and (d–e) showing element distribution in spinel LiNi_{0.5}Mn_{1.5}O₄. The Li frequency distribution of Li_{1.2}Ni_{0.2}Mn_{0.6}O₂ is shown in (g) along with the Pearson coefficient and (h) shows the frequency distribution of Li in LiNi_{0.5}Mn_{1.5}O₄ (adapted from Devaraj *et al.*) [223].

of APT for 3-D nanoscale compositional analysis [222–225]. The lithium- and sodium-ion battery technologies rely on fast shuttling of Li or Na ions across electrodes and electrolyte during electrochemical cycling. Both of these elements, having low atomic numbers, are very difficult to quantitatively image using traditional electron microscopy techniques. At the same time, APT is ideal for studying such light elements with high spatial resolution and high mass sensitivity, and hence can have a critical role in high-resolution compositional characterisation of battery materials. So far, there have been demonstrations of successful APT analysis of a LiCoO₂ thin film deposited on a pre-sharpened W needle [222] and of larger LiCoO₂ particles both before and after cycling in a battery, revealing compositional heterogeneities in Li distribution [223]. Another study by Santhanagopalan *et al.* compared the effect of the wavelength of laser used for APT on the accuracy of composition quantification of LiFePO₄, a common Li-ion battery cathode material [225]. Based on that study, the ability of UV laser-assisted APT to accurately quantify Li, Fe, and P with minor loss of O was established. Even more recently, APT was used to visualise the nanoscale

distribution of Li in two advanced Li-ion battery cathodes: layered $\text{Li}_{1.2}\text{Ni}_{0.2}\text{Mn}_{0.6}\text{O}_2$ and spinel $\text{LiNi}_{0.5}\text{Mn}_{1.5}\text{O}_4$ cathode nanoparticles [224]. Using APT, the presence of a non-uniform distribution of Li in both as-fabricated and cycled layered $\text{Li}_{1.2}\text{Ni}_{0.2}\text{Mn}_{0.6}\text{O}_2$ was identified with a significant loss of Li as a result of cycling, while a rather uniform distribution of Li was reported in spinel $\text{LiNi}_{0.5}\text{Mn}_{1.5}\text{O}_4$ cathodes (Figure 22). This was achieved by using a modified FIB-based nanoparticle lift-out method, similar to what is given in Figure 5 for preparing APT specimens of nanoparticles followed by UV laser-assisted APT experiments. This unique application of APT for characterising the quantitative and spatially resolved distribution of light elements in battery materials is expected to reach wide scale adoption for energy storage research in the near future.

Catalyst materials

Recently, there have been multiple demonstrations of the power of APT in quantifying and visualising the nanoscale chemistry of fully metallic alloy catalysts, [226–230] metallic core-shell nanoparticle catalysts, [231,232] and catalysts consisting of metal nanoparticles distributed on supports [32,109,233,234] or mesoporous catalyst materials like zeolites [235,236]. Often, the nanoscale composition of catalyst materials as a function of different synthesis methods or as a function of the catalytic environment has a pronounced influence on the catalytic performance. At present, most other techniques like aberration-corrected STEM imaging or x-ray-based techniques lack the spatial resolution and quantification capability that sets apart APT as a unique capability for catalyst material characterisation. A direct integration of an APT system with an environmental chamber can additionally permit exploring the thermodynamics and kinetics related to oxidation and reduction of catalyst materials in different gas environments [226–230,236]. New methodologies for preparing APT specimens from nanoparticles, either as-is or as dispersed on a support by electrophoresis, or modified FIB-based specimen preparation methods permit direct APT analysis of core-

shell and alloy catalyst nanoparticles [32,231,232]. An example of this is provided in Figure 23, where Li *et al.* used electrophoresis-based sample preparation followed by APT to analyse the composition of carbon-supported Pt–Co nanoparticles, including the distribution of undesirable impurities like Na at a particle-to-particle level spatial resolution [32]. Another significant area where APT can contribute heavily is in high spatial resolution compositional characterisation of mesoporous materials like zeolites, where electron beam sensitivity limits the capabilities of analytical TEM [235]. Even though these new demonstrations are laying the foundation for increased use of APT for catalyst material analysis, issues like local magnification artefacts during analysis of metal nanoparticles supported on oxides or other support materials will need to be understood and corrected in the reconstruction of APT data to fully achieve the ultimate goal of characterisation of a wide range of industrially relevant catalyst materials using APT. This is especially important in the case of metal nanoparticles supported on porous oxide substrates. Correlative microscopy and developments in APT simulations are expected to heavily contribute to such advances for wider scale adoption of APT for catalyst material characterisation.

Application of APT in geological materials

The 3-D composition mapping capability with atomic-scale resolution and part-per-million sensitivity of APT [24] brings the promising capability to study the chemical distribution of major and trace elements at atomic scale. In addition, with the ability to discriminate among isotopes, this technique has been applied to provide information about geologic dates of terrestrial minerals as well as the origins of extraterrestrial samples.

Recently, APT was introduced to the field of cosmochemistry, [237] which is focused on the study of the solar system, its formation, its history and the process that shaped the planets. The primary advantage of APT is that it can provide chemical information at atomic-scale spatial resolution in three dimensions and parts-per-million detection sensitivity, allowing

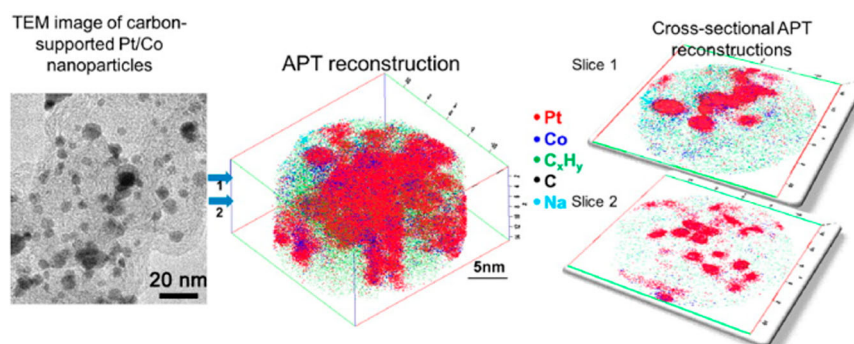


Figure 23. TEM images and APT results of carbon-supported Pt–Co nanoparticles (adapted from Li *et al.* [32]).

the study of very small extraterrestrial samples. APT analysis on presolar SiC grains was first reported by Heck and Stadermann [238,239]. Further study of an individual presolar SiC grain using APT shows that Al, at a concentration of ~ 280 at. ppm, is present in bands and extends throughout the volume of the grain [240]. In addition, researchers studied small size (~ 3 nm) [241] meteoritic nanodiamonds [239,240,242]. These studies show the ability of APT to consistently provide C isotopic compositions within analytical uncertainties from individual nanodiamonds. This information will help address outstanding issues in understanding the origin of nanodiamonds. In addition to the presolar SiC grains and meteoritic nanodiamonds, researchers have also explored presolar graphites, oxides, and silicates. However, this technique still requires development from two aspects: (1) the procedure for background correction and instrumental

bias correction needs to be standardised to allow consistent and accurate composition analysis, (2) sample preparation for study of loose powder needs to be optimised, such as the selection of a host matrix.

Compositional and isotopic structure analysis at subnanometre resolution is not only important in cosmochemistry but also in geochronology. Recently, geoscientists confirmed the dating of 4.4 gigayears (Gyr) old zircon using the radiogenic Pb mobility in zircon [243]. The APT data revealed ~ 10 nm concentrated clusters of radiogenic Pb isolated from a reheating event 3.4 Gyr ago and pushed the age of the zircon from 3.4 Gyr to 4.4 Gyr.

APT is also used in mineralogy. APT analysis on naturally occurring olivine has been reported with sub-nanometer spatial resolution [244,245]. However, the accuracy of the compositional analysis was not good due to the interaction of the laser pulse with

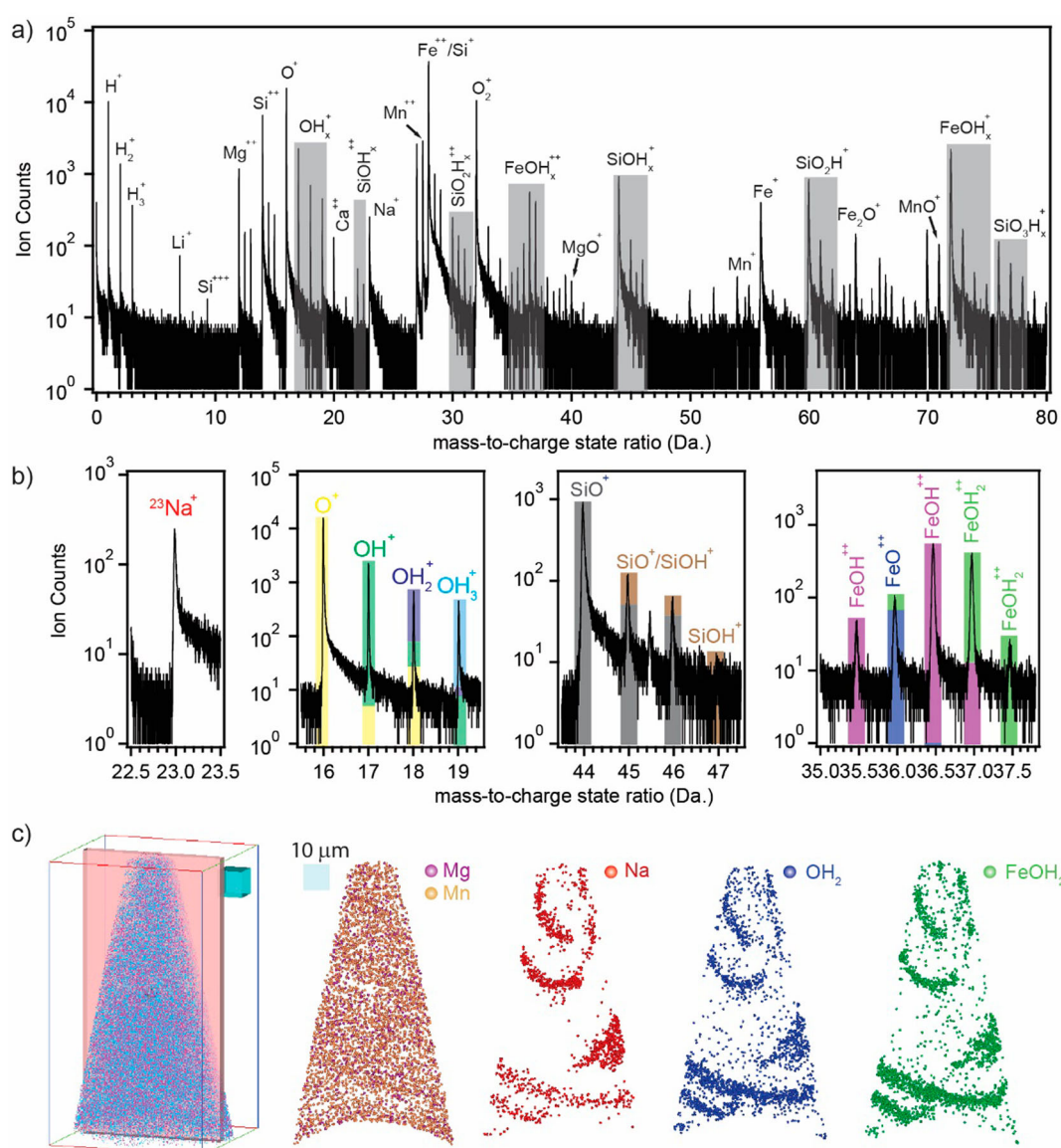


Figure 24. Mass spectra (a–b) and 3-D reconstruction map (c) of natural fayalite. Identification of the minor element, Na, and hydrated species, OH_x , $SiOH_x$, and $FeOH_x$, are highlighted in the mass spectrum in (b). For clarity, only 5% of Fe, Si, and O atoms are shown in (c). The distribution of Mg, Mn, Na, OH_2 , and $FeOH_2$ was taken from a sliced region with 10 nm thickness. The unit cube represents a volume of $10 \times 10 \times 10$ nm³ (Image courtesy J. Liu, PNNL).

the specimen of poor thermal conductivity. Overheating of specimens caused molecular evaporation, mass interference, and preferential loss of some species which led to inaccurate composition values. The accuracy of compositional analysis was improved with significant reduction in laser energy [244]. In addition, Liu reported an analysis of naturally occurring fayalite, revealing a heterogeneous channel-like distribution of Na spatially correlated with hydrated Si and Fe; this suggested water channel-like features in fayalite, shown in Figure 24, which may be an indication of $\text{Fe}(\text{OH})_2$ formation along associated dislocations. This study observed, for the first time, the distribution of hydrated components in fayalite using APT, which may advance the knowledge of geochemical processes.

APT for biological materials

Within a few decades following the invention of the FIM [246] (the predecessor of APT) in 1951, scientists had pursued a field ionisation approach to atomically image the structure and morphology of macromolecular biological materials, [247,248] leading to recent attempts to map their 3-D tomographic composition with modern pulsed-laser atom probes [249,250]. The ferritin protein has been the subject of previous FIM-based and more recent APT-based analyses for the following two reasons: (1) the iron-rich ferrihydrite core can provide a metallic signature in the mass spectrum to confirm field evaporation and detection of the protein; (2) the mineral core can also serve as a 3-D fiducial to delineate the relative composition of the conformal organic protein shell. From a scientific standpoint, the APT analysis of ferritin has the potential to reveal the subtle compositional distributions of phosphorus and other cations within and around the ferrihydrite mineral core, where the mapping of this distribution can provide insight into the presumed role of phosphorus in stabilising the ferrihydrite structure [251].

In order to perform a successful and meaningful 3-D tomographic analysis using APT that is broadly applicable to biological materials, some specimen requirements must be met: (1) the specimen must be able to be fashioned into the necessary needle-shaped geometry to facilitate thermally assisted field ionisation within the applied bias range; (2) the field ionisation should result in datasets of sufficient size and quality to be statistically and morphologically reliable. With regard to biological specimens, meeting these requirements is not trivial. Early attempts in the 1980s to prepare specimens consisted of the adsorption of biological macromolecules onto presharp metal needles. Although the morphological contours of the ferritin protein and other macromolecules were revealed, correlated compositional data via a mass

spectral analysis were never reported [252,253]. More recently, Green *et al.* repeated a similar analysis of ferritin adsorbed as a thin layer on metal needle tips, which resulted in a relatively small number of detected ion counts – below what is necessary to perform a reliable mass spectroscopic and tomographic analysis [254]. Following an approach using a FIB to prepare a needle-shaped specimen of ferritin embedded in a solidified NaCl buffer salt, Green *et al.* were able to field-evaporate the specimen with the assistance of a 532 nm wavelength laser. Mass spectral signatures associated with the protein shell were reported by comparison to a control analysis of the solid buffer NaCl salt without ferritin. However, gross mechanical deformation of the NaCl needle specimen made it a challenge to generate atomic-scale tomographic reconstructions that accurately depicted the expected structure of the embedded ferritin. Using a 355 nm laser, Gordon *et al.* analysed ferritin embedded in a sandwiched Au–Pd metal matrix by first depositing ferritin on Au–Pd-coated Si microposts followed by an additional Au–Pd overcoat and subsequent annular milling using a FIB to create needle specimens [255]. The tomographic 3-D distribution of a distinct ferritin molecule was reported, as evidenced by a cluster of Fe atoms from which a radial composition profile of Fe, O, and C delineated the interface between the inorganic ferrihydrite mineral core and carbon-rich protein shell. This is the first report of the 3-D composition of individual ferritin molecules.

In addition to compositional mapping of individual protein molecules, more complex biological systems, such as whole cells and organelle structures, have also been the subject of study with APT. Narayan *et al.* [256] reported the study of a whole mammalian cell. Freeze-dried human epithelial cells were encapsulated in gold and APT specimens were prepared using a FIB lift-out procedure. Although data were successfully collected from cellular tips, erratic evaporation events and the rough evaporating surface rendered the data quality too low for meaningful conclusions to be drawn.

Although the above results establish the viability of APT to detect and map macromolecular biological materials embedded in a matrix using APT analysis, the approach of embedding a biological material in either an inorganic (e.g. NaCl) or metallic (e.g. Au or Au–Pd) matrix does not seem to be the best choice considering the large difference in evaporation field between biological materials ($C \approx 100 \text{ V}\cdot\text{nm}^{-1}$) and the inorganic ($\text{Na} \approx 10 \text{ V}\cdot\text{nm}^{-1}$) or metallic ($\text{Au, Pt, Pd} \approx 40\text{--}55 \text{ V}\cdot\text{nm}^{-1}$) species. It is known that a large difference in evaporation fields can lead to significant differences in local magnification at the specimen surface and ultimately result in reconstruction artefacts [257] that can preclude an accurate reconstruction. A more logical approach would be to embed the macromolecular biological materials within an organic

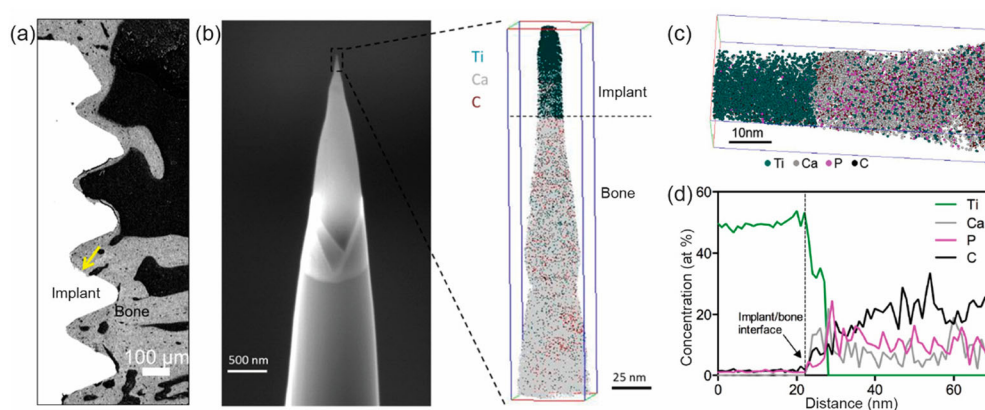


Figure 25. (a) Backscattered SEM images of bone–implant interface. The yellow arrow indicates the position where the lift-out was extracted. (b) SEM image of the sharpened tip, together with the APT reconstruction. Ti-containing ions are displayed in dark green, Ca-containing ions are grey, and C-containing ions are brown. (c) Magnified APT reconstruction displaying the direct contact between the Ca-containing inorganic bone mineral and Ti-containing implant surface. (d) 1-D concentration profiles of Ti, C, Ca, and P across the bone–implant interface (adapted from Karlsson *et al.* [259]).

matrix, such as a polymer, to better match the evaporation fields. A non-trivial challenge then lies in developing a strategy to spatially distinguish the carbon species originating from the biological material of interest from the carbon species making up the polymer matrix. Strategic isotopic labelling or choosing embedding matrices with specific compositions may provide the needed chemical contrast.

By far, the most impactful contributions of APT to biological materials have been reported in the analysis of biomineral tooth and bone tissues. Gordon and Joester [258] reported the study of the magnetite cusp of a chiton tooth using APT. APT analysis revealed the presence of 5–10 nm diameter organic fibres in the surrounding nanocrystalline magnetite (Fe_3O_4). Organic fibres were found to co-localise with either sodium or magnesium. Clustering of these cations in the fibre indicates a level of structural hierarchy that was previously undetected. The difference in chemical composition could possibly be associated with different functional roles in controlling fibre formation and matrix–mineral interactions. Proximity histograms showed that the interfaces between the mineral and the fibrous organic matrix were graded over 2–4 nm. Gordon *et al.* [259] subsequently analysed dentin and bone, similar biomineralised tissues that consist of hydroxylapatite nanocrystals and collagen. APT of dentin clearly revealed the fibrous nature of the collagenous organic matrix in dentin. Karlsson *et al.* [260] examined the nature of the complex interface between a titanium dental implant and the surrounding bone. Using APT, they were able to confirm that direct contact between inorganic bone mineral and the mesoporous titanium oxide-coated implant surface is formed without an organic interlayer, providing evidence in support of existing theories of osseointegration (Figure 25). Gordon *et al.* [261,262] proceeded to analyse the harder rodent dental enamel, a hierarchical tissue composed of hydroxylapatite NWs. Using

APT, they identified nanoscale heterogeneity in the distribution of inorganic ions and organic molecules in the hierarchical tissue that have a controlling influence on the resistance to acid corrosion and mechanical properties of the tissue. Using APT in combination with x-ray absorption spectroscopy, they identified Mg-substituted amorphous calcium phosphate at grain boundaries in unpigmented rodent enamel, while the surface layer of pigmented enamel was found to contain instead a mixture of intergranular ferrihydrite and amorphous iron–calcium phosphate, rendering it both harder and more resistant to acid attack. These findings provide fundamental new insight into the responsibility of enduring amorphous phases in the acid corrosion behaviour of dental enamel.

Future of APT

APT is certainly moving towards being established as a mainstream characterisation capability for a variety of materials similar to TEM or other well-established characterisation techniques. While APT is predominantly performed at research institutions, a growing number of industries are actively pursuing APT analysis of industrially relevant products. Adoption by industries also indicates increasing maturity of APT for material characterisation.

Developments to anticipate include new detectors that could push the detection limit closer to 100% and the possibility of achieving kinetic energy discrimination, permitting deconvolution of overlapping isotopes. Another significant development could be the commercial scale development of multimodal instruments with either a TEM or SEM column directly on an APT system or vice versa, providing real-time or intermittent imaging and/or diffraction to assess specimen shape and crystallography during APT analysis, which could significantly improve the reconstruction

accuracy for complex heterogeneous materials. A few research groups around the world are focusing their efforts towards such multimodal instruments at present.

Significant growth could also be expected within computationally guided APT reconstruction as well as interpretation. Many efficient computer simulation methods are under development to study the evaporation process of specimens in APT as well as the reconstruction process [90,263]. With the aid of correlative experimental work, the refinement of such simulations may produce more effective and accurate reconstruction methods.

Also there is significant ongoing discussion about the development of APT standards as a part of international standards organisations, which should help in establishing unified protocols for APT sample preparation, data collection processes, reconstructions and analysis and reporting of results across APT research groups worldwide. All these developments are expected to lay the foundation for a bright future of APT as a characterisation capability that can take not only material scientists but also researchers from a variety of disciplines, including geology, biology, and solid-state materials, closer to the ultimate goal of achieving the 3-D composition, structure, and chemical state atom by atom.

Acknowledgements

The main funding support for preparation of this review article was received from a laboratory directed research and development project in Pacific Northwest National Laboratory (PNNL) as a part of Chemical Imaging Initiative. PNNL is operated by Battelle Memorial Institute for the United States Department of Energy under Contract DE-AC05-76RLO1830. Some of the research was performed using FIB-SEM and APT instrumentation at the Environmental Molecular Sciences Laboratory, a national scientific user facility sponsored by the Department of Energy's Office of Biological and Environmental Research and located at PNNL. For detailed acknowledgements for all results from other previous publications reviewed here in this review article, readers are encouraged to check the original acknowledgement section in the cited publications.

Disclosure Statement

No potential conflict of interest was reported by the authors.

ORCID

David R. Diercks  <http://orcid.org/0000-0002-5138-0168>
R. Prakash Kolli  <http://orcid.org/0000-0003-1345-1735>

References

- [1] Muller EW, Panitz JA, McLane SB. Atom-probe field ion microscope. *Rev Sci Instrum.* 1968;39(1):83–86.
- [2] Kelly TF, Miller MK. Invited review article: atom probe tomography. *Rev Sci Instrum.* 2007;78(3):031101.
- [3] Kelly TF, Larson DJ. The second revolution in atom probe tomography. *MRS Bull.* 2012;37(2):150–158.
- [4] Panitz JA. Imaging atom-probe mass-spectroscopy. *Prog Surf Sci.* 1978;8(6):219–262.
- [5] Kellogg GL, Tsong TT. Pulsed laser-induced atom-probe mass-spectroscopy. *Ultramicroscopy.* 1980;5(2):259–260.
- [6] Kellogg GL. Pulsed laser atom-probe study of the dissociation of CO on Molybdenum. *Surf Sci.* 1981;111(2):205–213.
- [7] Kellogg GL. Field-ion microscopy and pulsed laser atom-probe mass-spectroscopy of insulating glasses. *J Appl Phys.* 1982;53(9):6383–6386.
- [8] Kingham DR. The post-ionization of field evaporated ions – a theoretical explanation of multiple charge states. *Surf Sci.* 1982;116(2):273–301.
- [9] Kellogg GL. Pulsed-laser atom probe mass-spectroscopy. *J Phys E Sci Instrum.* 1987;20(2):125–136.
- [10] Kellogg GL, Brenner SS. Field-ion microscopy and imaging atom-probe mass-spectroscopy of superconducting Yba2cu3o7-X. *Appl Phys Lett.* 1987;51(22):1851–1853.
- [11] Kellogg GL. Field ion microscopy and atom-probe mass-spectroscopy – techniques and selected applications. *Scanning Microsc.* 1988;2(4):1845–1852.
- [12] Kellogg GL, Brenner SS. Investigations of superconducting and non-superconducting Yba2cu3o7-X by field-ion microscopy, atom-probe mass-spectroscopy and field electron-emission. *J Phys-Paris.* 1988;49(C-6):465–470.
- [13] Bunton JH, Olson JD, Lenz DR, et al. Optimized laser thermal pulsing of atom probe tomography: LEAP 4000X. *Microsc Microanal.* 2010;16(S2):10–11.
- [14] Kelly TE, Gribb TT, Olson JD, et al. First data from a commercial local electrode atom probe (LEAP). *Microsc Microanal.* 2004;10(3):373–383.
- [15] Tsong TT. Field-ion image-formation. *Surf Sci.* 1978;70(1):211–233.
- [16] Kellogg GL, Tsong TT. Pulsed-laser atom-probe field-ion microscopy. *J Appl Phys.* 1980;51(2):1184–1193.
- [17] Hono K. Nanoscale microstructural analysis of metallic materials by atom probe field ion microscopy. *Prog Mat Sci.* 2002;47(6):621–729.
- [18] Schlesinger R, Oberdorfer C, Wurz R, et al. Design of a laser-assisted tomographic atom probe at Muumlnter University. *Rev Sci Instrum.* 2010;81(4):043705.
- [19] Gault B, Vurpillot F, Vella A, et al. Design of a femto-second laser assisted tomographic atom probe. *Rev Sci Instrum.* 2006;77(4).
- [20] Müller EW, Krishnaswamy SV. Energy deficits in pulsed field evaporation and deficit compensated atom-probe designs. *Rev Sci Instrum.* 1974;45(9):1053–1059.
- [21] Waugh AR, Richardson CH, Jenkins R. Apfim-200 – a reflectron-based atom probe. *Surf Sci.* 1992;266(1–3):501–505.
- [22] Cerezo A, Godfrey TJ, Sijbrandij SJ, et al. Performance of an energy-compensated three-dimensional atom probe. *Rev Sci Instrum.* 1998;69(1):49–58.
- [23] Jagutzki O, Cerezo A, Czausch A, et al. Multiple hit readout of a microchannel plate detector with a three-layer delay-line anode. *IEEE T Nucl Sci.* 2002;49(5):2477–2483.

- [24] Miller MK. Atom probe tomography: analysis at the atomic level. New York: Kluwer Academic/Plenum Publishers; 2000.
- [25] Gault B, Moody MP, Cairney JM, et al. Atom probe microscopy. XIII + 372. New York (NY): Springer-Verlag; 2012.
- [26] Larson DJ, Foord DT, Petford-Long AK, et al. Field-ion specimen preparation using focused ion-beam milling. *Ultramicroscopy*. 1999;79(1–4):287–293.
- [27] Thompson K, Lawrence D, Larson DJ, et al. In situ site-specific specimen preparation for atom probe tomography. *Ultramicroscopy*. 2007;107(2–3):131–139.
- [28] Thompson K, Gorman B, Larson D, et al. Minimization of Ga induced FIB damage using low energy clean-up. *Microsc Microanal*. 2006;12 (Supplement S02):1736–1737.
- [29] Madaan N, Bao J, Nandasiri M, et al. Impact of dynamic specimen shape evolution on the atom probe tomography results of doped epitaxial oxide multilayers: comparison of experiment and simulation. *Appl Phys Lett*. 2015;107(9):091601.
- [30] Devaraj A, Szymanski C, Yan P, et al. Nanoscale characterization of Li-ion battery cathode nanoparticles by atom probe tomography correlated with transmission electron microscopy and scanning transmission X-Ray microscopy. *Microsc Microanal*. 2015;21(Supplement S3):685–686.
- [31] Larson DJ, Giddings AD, Wu Y, et al. Encapsulation method for atom probe tomography analysis of nanoparticles. *Ultramicroscopy*. 2015;159(2):420–426.
- [32] Li T, Bagot PAJ, Christian E, et al. Atomic imaging of carbon-supported Pt, Pt/Co, and Ir@Pt nanocatalysts by atom-probe tomography. *Acs Catal*. 2014;4(2):695–702.
- [33] Felfer P, Li T, Eder K, et al. New approaches to nanoparticle sample fabrication for atom probe tomography. *Ultramicroscopy*. 2015;159(2):413–419.
- [34] Fasth JE, Loberg B, Norden H. Preparation of contamination-free Tungsten specimens for field-ion microscope. *J Sci Instrum*. 1967;44(12):1044.
- [35] Norden H, Bowkett KM. Electron microscope holders for viewing thin wire specimens and field-ion microscope tips. *J Sci Instrum*. 1967;44(3):238–240.
- [36] Henjered A, Norden H. A controlled specimen preparation technique for interface studies with atom-probe field-ion microscopy. *J Phys E-Sci Instrum*. 1983;16(7):617–619.
- [37] Krakauer BW, Seidman DN. Systematic procedures for atom-probe field-ion microscopy studies of grain-boundary segregation. *Rev Sci Instrum*. 1992;63(9):4071–4079.
- [38] Arslan I, Marquis EA, Homer M, et al. Towards better 3-D reconstructions by combining electron tomography and atom-probe tomography. *Ultramicroscopy*. 2008;108(12):1579–1585.
- [39] Gorman BP, Diericks D, Salmon N, et al. Hardware and techniques for correlative TEM and atom probe analysis. *Microscopy Today*. 2008;16(4):42–48.
- [40] Bennett SE, Saxey DW, Kappers MJ, et al. Atom probe tomography assessment of the impact of electron beam exposure on InxGa1-xN/GaN quantum wells. *Appl Phys Lett*. 2011;99(2):021906.
- [41] Felfer PJ, Alam T, Ringer SP, et al. A reproducible method for damage-free site-specific preparation of atom probe tips from interfaces. *Microsc Res Techniq*. 2012;75(4):484–491.
- [42] Herbig M, Choi P, Raabe D. Combining structural and chemical information at the nanometer scale by correlative transmission electron microscopy and atom probe tomography. *Ultramicroscopy*. 2015;153:32–39.
- [43] Wagner RS, Ellis WC. Vapor-liquid-solid mechanism of single crystal growth (new method growth catalysis from impurity whisker epitaxial + large crystals SIE). *Appl Phys Lett*. 1964;4(5), 89.
- [44] Lauhon LJ, Gudiksen MS, Lieber CM. Semiconductor nanowire heterostructures. *Philos T Roy Soc A*. 2004;362(1819):1247–1260.
- [45] Perea DE, Allen JE, May SJ, et al. Three-dimensional nanoscale composition mapping of semiconductor nanowires. *Nano Lett*. 2006;6(2):181–185.
- [46] Perea DE, Lensch JL, May SJ, et al. Composition analysis of single semiconductor nanowires using pulsed-laser atom probe tomography. *Appl Phys A-Mater*. 2006;85(3):271–275.
- [47] Perea DE, Wijaya E, Lensch-Falk JL, et al. Tomographic analysis of dilute impurities in semiconductor nanostructures. *J Solid State Chem*. 2008;181(7):1642–1649.
- [48] Xu T, Nys JP, Granddier B, et al. Growth of Si nanowires on micropillars for the study of their dopant distribution by atom probe tomography. *J Vac Sci Technol B*. 2008;26(6):1960–1963.
- [49] Diercks DR, Gorman BP, Cheung CL, et al. Techniques for consecutive TEM and atom probe tomography analysis of nanowires. *Microsc Microanal*. 2009;15(S2):254–255.
- [50] Blumtritt H, Isheim D, Senz S, et al. Preparation of nanowire specimens for laser-assisted atom probe tomography. *Nanotechnology*. 2014;25(43):435704.
- [51] Padalkar S, Riley JR, Li QM, et al. Lift-out procedures for atom probe tomography targeting nanoscale features in core-shell nanowire heterostructures. *Phys Status Solidi C*. 2014;11(3–4):656–661.
- [52] Prosa TJ, Alvis R, Tsakalakos L, et al. Characterization of dilute species within CVD-grown silicon nanowires doped using trimethylboron: protected lift-out specimen preparation for atom probe tomography. *J Microsc-Oxford*. 2010;239(2):92–98.
- [53] Dawahre N, Shen G, Balci S, et al. Atom probe tomography of Zinc oxide nanowires. *J Electron Mater*. 2012;41(5):801–808.
- [54] Mangelinck D, Panciera F, Hoummada K, et al. Atom probe tomography for advanced metallization. *Microelectron Eng*. 2014;120:19–33.
- [55] Larson DJ, Prosa TJ, Ulfeg RM, et al. Local electrode atom probe tomography: a user's guide. New York: Springer; 2013.
- [56] Miller MK, Smith GDW. An atom probe study of the anomalous field evaporation of alloys containing Silicon. *J Vac Sci Technol*. 1981;19:57–62.
- [57] Miller MK, Russell KF. Performance of a local electrode atom probe. *Surf Interf Anal*. 2007;39:262–267.
- [58] Yamaguchi Y, Takahashi J, Kawakami K. The study of quantitiveness in atom probe analysis of alloying elements in steel. *Ultramicroscopy*. 2009;109:541–544.
- [59] Zhou Y, Booth-Morrison C, Seidman DN. On the field evaporation behavior of a model Ni-Al-Cr superalloy studied by picosecond pulsed-laser atom-probe tomography. *Microsc Microanal*. 2008;14:571–580.
- [60] Tang F, Gault B, Ringer SP, et al. Optimization of pulsed laser atom probe (PLAP) for the analysis of

- nanocomposite Ti-Si-N films. *Ultramicroscopy*. 2010;110:836–843.
- [61] Tu Y, Plotnikov EY, Seidman DN. A model Ni-Al-Mo superalloy studied by ultraviolet pulsed-laser-assisted local-electrode atom-probe tomography. *Microsc Microanal*. 2015;21:480–490.
- [62] Valderrama B, Henderson HB, Gan J, et al. Influence of instrument conditions on the evaporation behavior of uranium dioxide with UV laser-assisted atom probe tomography. *J Nucl Mater*. 2015;459:37–43.
- [63] Diercks DR, Gorman BP. Nanoscale measurement of laser-induced temperature rise and field evaporation effects in CdTe and GaN. *J Phys Chem C*. 2015;119:20623–20631.
- [64] Thuvander M, Weidow J, Angseryd J, et al. Quantitative atom probe analysis of carbides. *Ultramicroscopy*. 2011;111:604–608.
- [65] Meisenkothen F, Steel EB, Prosa TJ, et al. Effects of detector dead-time on quantitative analyses involving boron and multi-hit detection events in atom probe tomography. *Ultramicroscopy*. 2015;159(Part 1):101–111.
- [66] Stephan T, Heck PR, Isheim D, et al. Correction of dead time effects in laser-induced desorption time-of-flight mass spectrometry: applications in atom probe tomography. *Int J Mass Spectrom*. 2015;379:46–51.
- [67] Müller M, Smith GDW, Gault B, et al. Compositional nonuniformities in pulsed laser atom probe tomography analysis of compound semiconductors. *J Appl Phys*. 2012;111:064908.
- [68] Kelly TF. Kinetic-energy discrimination for atom probe tomography. *Microsc Microanal*. 2011;17:1–14.
- [69] Saxey DW. Correlated ion analysis and the interpretation of atom probe mass spectra. *Ultramicroscopy*. 2011;111:473–479.
- [70] Vurpillot F, Da Costa G, Menand A, et al. Structural analyses in three-dimensional atom probe: a Fourier transform approach. *J Microsc-Oxford*. 2001;203:295–302.
- [71] Geiser BP, Kelly TF, Larson DJ, et al. Spatial distribution maps for atom probe tomography. *Microsc Microanal*. 2007;13(6):437–447.
- [72] Birdseye PJ, Smith DA. The electric field and the stress on a field-ion specimen. *Surf Sci*. 1970;23:198–210.
- [73] Mikhailovskij IM, Wanderka N, Storizhko VE, et al. A new approach for explanation of specimen rupture under high electric field. *Ultramicroscopy*. 2009;109:480–485.
- [74] Hono K, Ohkubo T, Chen YM, et al. Broadening the applications of the atom probe technique by ultraviolet femtosecond laser. *Ultramicroscopy*. 2011;111:576–583.
- [75] Kirchhofer R, Teague MC, Gorman BP. Thermal effects on mass and spatial resolution during laser pulse atom probe tomography of cerium oxide. *J Nucl Mater*. 2013;436:23–28.
- [76] Kolli RP, Seidman DN. Co-precipitated and collocated carbides and Cu-rich precipitates in a Fe-Cu steel characterized by atom-probe tomography. *Microsc Microanal*. 2014;20:1727–1739.
- [77] Bunton JH, Olson JD, Lenz D, et al. Advances in pulsed-laser atom probe: instrument and specimen design for optimum performance. *Microsc Microanal*. 2007;13:418–427.
- [78] Houard J, Vella A, Vurpillot F, et al. Conditions to cancel the laser polarization dependence of a subwavelength tip. *Appl Phys Lett*. 2009;94:121905.
- [79] Gault B, Danoix F, Hoummada K, et al. Impact of directional walk on atom probe microanalysis. *Ultramicroscopy*. 2012;113:182–191.
- [80] Vella A. On the interaction of an ultra-fast laser with a nanometric tip by laser assisted atom probe tomography: A review. *Ultramicroscopy*. 2013;132:5–18.
- [81] Prosa TJ, Lawrence D, Olson D, et al. Experimental evaluation of conditions affecting specimen survivability. *Microsc Microanal*. 2015;21:849–850.
- [82] Discussion: 'LEAP User's Meeting', Cameca LEAP User's Meeting, June, 2015, 2015.
- [83] Prosa TJ, Lenz DR, Payne TR, et al. 'Novel Evaporation Control Concepts', *Frontiers of Characterization and Metrology for Nanoelectronics*, 2013 Mar 25–28; 2013. p. 269–272.
- [84] Bas P, Bostel A, Deconihout B, et al. A general protocol for the reconstruction of 3D atom probe data. *Appl Surf Sci*. 1995;87–88:298–304.
- [85] Geiser BP, Larson DJ, Oltman E, et al. Wide-field-of-view atom probe reconstruction. *Microsc Microanal*. 2009;15(S2):292–293.
- [86] Martin AJ, Weng W, Zhu Z, et al. Cross-sectional atom probe tomography sample preparation for improved analysis of fins on SOI. *Ultramicroscopy*. 2016;161:105–109.
- [87] Vurpillot F, Gault B, Geiser BP, et al. Reconstructing atom probe data: a review. *Ultramicroscopy*. 2013;132:19–30.
- [88] Gault B, Haley D, de Geuser F, et al. Advances in the reconstruction of atom probe tomography data. *Ultramicroscopy*. 2011;111:448–457.
- [89] Miller MK, Forbes RG. Atom-probe tomography: the local electrode atom probe. 423. New York (NY): Springer; 2014.
- [90] Larson DJ, Gault B, Geiser BP, et al. Atom probe tomography spatial reconstruction: status and directions. *Curr Opin Solid St M*. 2013;17(5):236–247.
- [91] Moody MP, Gault B, Stephenson LT, et al. Qualification of the tomographic reconstruction in atom probe by advanced spatial distribution map techniques. *Ultramicroscopy*. 2009;109:815–824.
- [92] Stephenson LT, Moody MP, Liddicoat PV, et al. New techniques for the analysis of fine-scaled clustering phenomena within atom probe tomography (APT) data. *Microsc Microanal*. 2007;13:448–463.
- [93] Vurpillot F, Larson D, Cerezo A. Improvement of multilayer analyses with a three-dimensional atom probe. *Surf Interf Anal*. 2004;36:552–558.
- [94] Vurpillot F, Gruber M, Da Costa G, et al. Pragmatic reconstruction methods in atom probe tomography. *Ultramicroscopy*. 2011;111:1286–1294.
- [95] De Geuser F, Lefebvre W, Danoix F, et al. An improved reconstruction procedure for the correction of local magnification effects in three-dimensional atom-probe. *Surf Interf Anal*. 2007;39:268–272.
- [96] Larson DJ, Geiser BP, Prosa TJ, et al. On the use of simulated field-evaporated specimen apex shapes in atom probe tomography data reconstruction. *Microsc Microanal*. 2012;18:953–963.
- [97] Moody MP, Gault B, Stephenson LT, et al. Lattice rectification in atom probe tomography: toward true three-dimensional atomic microscopy. *Microsc Microanal*. 2011;17:226–239.

- [98] Hyde JM, Cerezo A, Setna RP, et al. Lateral and depth scale calibration of the position sensitive atom probe. *Appl Surf Sci.* **1994**;76-77:382–391.
- [99] Gault B, de Geuser F, Stephenson LT, et al. Estimation of the reconstruction parameters for atom probe tomography. *Microsc Microanal.* **2008**;14:296–305.
- [100] Prosa TJ, Olson D, Geiser B, et al. Analysis of implanted silicon dopant profiles. *Ultramicroscopy.* **2013**;132:179–185.
- [101] Prosa TJ, Geiser BP, Reinhard D, et al. Approaches for promoting accurate atom probe reconstructions. *Microsc. Microanal.* **2016**;22(S3):664–665.
- [102] Gorman BP, Puthucode A, Diercks DR, et al. Cross-correlative TEM and atom probe analysis of partial crystallisation in NiNbSn metallic glasses. *Mater Sci Technol.* **2008**;24:682–688.
- [103] Shariq A, Mutas S, Wedderhoff K, et al. Investigations of field-evaporated end forms in voltage- and laser-pulsed atom probe tomography. *Ultramicroscopy.* **2009**;109:472–479.
- [104] Rolland N, Larson DJ, Geiser BP, et al. An analytical model accounting for tip shape evolution during atom probe analysis of heterogeneous materials. *Ultramicroscopy.* **2015**;159:195–201.
- [105] Gault B, Loi SH, Araullo-Peters V, et al. Dynamic reconstruction for atom probe tomography. *Ultramicroscopy.* **2011**;111:1619–1624.
- [106] Haley D, Petersen T, Ringer SP, et al. Atom probe trajectory mapping using experimental tip shape measurements. *J Microsc-Oxford.* **2011**;244:170–180.
- [107] Petersen TC, Ringer SP. An electron tomography algorithm for reconstructing 3D morphology using surface tangents of projected scattering interfaces. *Comput Phys Commun.* **2010**;181:676.
- [108] Larson DJ, Geiser BP, Prosa TJ, et al. Improvements in planar feature reconstructions in atom probe tomography. *J Microsc-Oxford.* **2011**;243:15.
- [109] Devaraj A, Colby R, Vurpillot F, et al. Understanding atom probe tomography of oxide-supported metal nanoparticles by correlation with atomic-resolution electron microscopy and field evaporation simulation. *J Phys Chem Lett.* **2014**;5(8):1361–1367.
- [110] Papazian JM. The preparation of field-ion-microscope specimens containing grain boundaries. *J Microsc-Oxford.* **1971**;94(1):63–67.
- [111] Devaraj A, Colby R, Hess WP, et al. Role of photoexcitation and field ionization in the measurement of accurate oxide stoichiometry by laser-assisted atom probe tomography. *J Phys Chem Lett.* **2013**;4(6):993–998.
- [112] Devaraj A, Nag S, Banerjee R. Alpha phase precipitation from phase-separated beta phase in a model Ti-Mo-Al alloy studied by direct coupling of transmission electron microscopy and atom probe tomography. *Scripta Mater.* **2013**;69(7):513–516.
- [113] Kuzmina M, Herbig M, Ponge D, et al. Linear complexes: confined chemical and structural states at dislocations. *Science.* **2015**;349(6252):1080–1083.
- [114] Hartshorne MI, Isheim D, Seidman DN, et al. Specimen preparation for correlating transmission electron microscopy and atom probe tomography of mesoscale features. *Ultramicroscopy.* **2014**;147:25–32.
- [115] Williams CA, Marquis EA, Cerezo A, et al. Nanoscale characterisation of ODS–Eurofer 97 steel: an atom-probe tomography study. *J Nucl Mater.* **2010**;400(1):37–45.
- [116] Diercks DR, Gorman BP, Manerbino A, et al. Atom probe tomography of Yttrium-Doped Barium–Cerium–Zirconium Oxide with NiO addition. *J Am Ceram Soc.* **2014**;97(10):3301–3306.
- [117] Schreiber DK, Olszta MJ, Bruemmer SM. Directly correlated transmission electron microscopy and atom probe tomography of grain boundary oxidation in a Ni–Al binary alloy exposed to high-temperature water. *Scripta Mater.* **2013**;69(7):509–512.
- [118] Baik SI, Yin X, Seidman DN. Correlative atom-probe tomography and transmission electron microscope study of a chemical transition in a spinel on an oxidized nickel-based superalloy. *Scripta Mater.* **2013**;68(11):909–912.
- [119] Lee JH, Lee BH, Kim YT, et al. Study of vertical Si/SiO₂ interface using laser-assisted atom probe tomography and transmission electron microscopy. *Micron.* **2014**;58:32–37.
- [120] Herbig M, Raabe D, Li YJ, et al. Atomic-scale quantification of grain boundary segregation in nanocrystalline material. *Phys Rev Lett.* **2014**;112(12):245701.
- [121] Stoffers A, Cojocar-Mirédin O, Seifert W, et al. Grain boundary segregation in multicrystalline silicon: correlative characterization by EBSD, EBIC, and atom probe tomography. *Prog Photovoltaics Res Appl.* **2015**;23:1742–1753.
- [122] Nag S, Devaraj A, Srinivasan R, et al. Novel mixed-mode phase transition involving a composition-dependent displacive component. *Phys Rev Lett.* **2011**;106(24).
- [123] Ng HP, Nandwana P, Devaraj A, et al. Conjugated precipitation of twin-related α and Ti₂Cu phases in a Ti–25V–3Cu alloy. *Acta Materialia.* **2015**;84:457–471.
- [124] Devaraj A, Joshi VV, Srivastava A, et al. A low-cost hierarchical nanostructured beta-titanium alloy with high strength. *Nat Commun.* **2016**;7:11176.
- [125] Devaraj A, Nag S, Srinivasan R, et al. Experimental evidence of concurrent compositional and structural instabilities leading to omega precipitation in titanium-molybdenum alloys. *Acta Materialia.* **2012**;60(2):596–609.
- [126] Ng HP, Devaraj A, Nag S, et al. Phase separation and formation of omega phase in the beta matrix of a Ti–V–Cu alloy. *Acta Materialia.* **2011**;59(8):2981–2991.
- [127] Kolli RP, Herzing AA, Ankem S. Characterization of yttrium-rich precipitates in a titanium alloy weld. *Mater Charact.* **2016**;122:30–35.
- [128] Yang F, Coughlin DR, Phillips PJ, et al. Structure analysis of a precipitate phase in an Ni-rich high-temperature NiTiHf shape memory alloy. *Acta Mater.* **2013**;61(9):3335–3346.
- [129] Mao Z, Sudbrack CK, Yoon KE, et al. The mechanism of morphogenesis in a phase-separating concentrated multicomponent alloy. *Nat Mater.* **2007**;6(3):210–216.
- [130] Sudbrack CK, Noebe RD, Seidman DN. Compositional pathways and capillary effects during isothermal precipitation in a nondilute Ni–Al–Cr alloy. *Acta Materialia.* **2007**;55(1):119–130.
- [131] Sudbrack CK, Yoon KE, Noebe RD, et al. Temporal evolution of the nanostructure and phase compositions in a model Ni–Al–Cr alloy. *Acta Materialia.* **2006**;54(12):3199–3210.
- [132] Kolli RP, Seidman DN. The temporal evolution of the decomposition of a concentrated multicomponent

- Fe-Cu-based steel. *Acta Materialia*. 2008;56(9):2073–2088.
- [133] Kolli RP, Wojes RM, Zaucha S, et al. A subnanoscale study of the nucleation, growth, and coarsening kinetics of Cu-rich precipitates in a multicomponent Fe-Cu based steel. *Int J Mater Res*. 2008;99(5):513–527.
- [134] Kolli RP, Seidman DN. Coarsening kinetics of Cu-rich precipitates in a concentrated multicomponent Fe-Cu based steel. *Int J Mater Res*. 2011;102(9):1115–1124.
- [135] Saha A, Jung J, Olson GB. Prototype evaluation of transformation toughened blast resistant naval hull steels: Part II. *J Comput-Aided Mater*. 2007;14(2):201–233.
- [136] Kolli RP, Seidman DN. Comparison of compositional and morphological atom-probe tomography analyses for a multicomponent Fe-Cu steel. *Microsc Microanal*. 2007;13(4):272–284.
- [137] Kolli RP, Mao Z, Seidman DN, et al. Identification of a Ni(0.5)(Al(0.5-x)Mn(x)) B2 phase at the heterophase interfaces of Cu-rich precipitates in an alpha-Fe matrix. *Appl Phys Lett*. 2007;91(24):241903.
- [138] Marquis EA, Seidman DN, Asta M, et al. Mg segregation at Al/Al₃Sc heterophase interfaces on an atomic scale: experiments and computations. *Phys Rev Lett*. 2003;91(3):036101.
- [139] Heinrich A, Al-Kassab T, Kirchheim R. Investigation of the early stages of decomposition of Cu-0.7at.% Fe with the tomographic atom probe. *Mat Sci Eng A-Struct*. 2003;353(1–2):92–98.
- [140] Vaumousse D, Cerezo A, Warren PJ. A procedure for quantification of precipitate microstructures from three-dimensional atom probe data. *Ultramicroscopy*. 2003;95(1–4):215–221.
- [141] Hellman OC, Vandenbroucke JA, Rusing J, et al. Analysis of three-dimensional atom-probe data by the proximity histogram. *Microsc Microanal*. 2000;6(5):437–444.
- [142] Hellman O, Vandenbroucke J, du Rivage JB, et al. Application software for data analysis for three-dimensional atom probe microscopy. *Mat Sci Eng A-Struct*. 2002;327(1):29–33.
- [143] Hellman OC, du Rivage JB, Seidman DN. Efficient sampling for three-dimensional atom probe microscopy data. *Ultramicroscopy*. 2003;95(1–4):199–205.
- [144] Marquis EA, Hyde JM. Applications of atom-probe tomography to the characterisation of solute behaviours. *Mat Sci Eng R*. 2010;69(4–5):37–62.
- [145] Miller MK, Kenik EA. Atom probe tomography: a technique for nanoscale characterization. *Microsc Microanal*. 2004;10(3):336–341.
- [146] Miller MK. Contributions of atom probe tomography to the understanding of nickel-based superalloys. *Micron*. 2001;32(8):757–764.
- [147] Meher S, Yan HY, Nag S, et al. Solute partitioning and site preference in gamma/gamma' cobalt-base alloys. *Scripta Mater*. 2012;67(10):850–853.
- [148] Meher S, Nag S, Tiley J, et al. Coarsening kinetics of gamma' precipitates in cobalt-base alloys. *Acta Materialia*. 2013;61(11):4266–4276.
- [149] Gault B, Cui XY, Moody MP, et al. Atom probe microscopy investigation of Mg site occupancy within delta' precipitates in an Al-Mg-Li alloy. *Scripta Mater*. 2012;66(11):903–906.
- [150] Blavette D, Cadel E, Deconihout B. The role of the atom probe in the study of nickel-based superalloys. *Mater Charact*. 2000;44(1–2):133–157.
- [151] Hono K, Chiba A, Sakurai T, et al. Determination of site occupation probability of Cu in Ni3Al by atom-probe field-ion microscopy. *Acta Metall Mater*. 1992;40(3):419–425.
- [152] Rademacher T, Al-Kassab T, Deges J, et al. Ordering and site occupancy of D0(3) ordered Fe3Al-5 at%Cr evaluated by means of atom probe tomography. *Ultramicroscopy*. 2011;111(6):719–724.
- [153] Gault B, Moody MP, Cairney JM, et al. Atom probe crystallography. *Mater Today*. 2012;15(9):378–386.
- [154] Araullo-Peters VJ, Gault B, Shrestha SL, et al. Atom probe crystallography: atomic-scale 3-D orientation mapping. *Scripta Mater*. 2012;66(11):907–910.
- [155] Ceguerra AV, Breen AJ, Stephenson LT, et al. The rise of computational techniques in atom probe microscopy. *Curr Opin Solid St M*. 2013;17(5):224–235.
- [156] Moody MP, Tang FZ, Gault B, et al. Atom probe crystallography: characterization of grain boundary orientation relationships in nanocrystalline aluminium. *Ultramicroscopy*. 2011;111(6):493–499.
- [157] Meher S, Nandwana P, Rojhirunsakool T, et al. Probing the crystallography of ordered phases by coupling of orientation microscopy with atom probe tomography. *Ultramicroscopy*. 2015;148:67–74.
- [158] Meher S, Rojhirunsakool T, Nandwana P, et al. Determination of solute site occupancies within gamma' precipitates in nickel-base superalloys via orientation-specific atom probe tomography. *Ultramicroscopy*. 2015;159(2):272–277.
- [159] Meher S, Banerjee R. Partitioning and site occupancy of Ta and Mo in Co-base gamma/gamma' alloys studied by atom probe tomography. *Intermetallics*. 2014;49:138–142.
- [160] Aranda MM, Rementeria R, Poplawsky J, et al. The role of C and Mn at the austenite/pearlite reaction front during non-steady-state pearlite growth in a Fe-C-Mn steel. *Scripta Mater*. 2015;104:67–70.
- [161] Tu YY, Mao ZG, Zhang Q, et al. Atomistic interaction between silicon and manganese in pearlitic steel: combined atom probe tomography and first-principle calculations. *Mater Lett*. 2014;134:84–86.
- [162] Contieri RJ, Lopes ESN, Caram R, et al. Effects of cooling rate on the microstructure and solute partitioning in near eutectoid Ti-Cu alloys. *Philos Mag*. 2014;94(21):2350–2371.
- [163] Seol JB, Raabe D, Choi P, et al. Direct evidence for the formation of ordered carbides in a ferrite-based low-density Fe-Mn-Al-C alloy studied by transmission electron microscopy and atom probe tomography. *Scripta Mater*. 2013;68(6):348–353.
- [164] Devaraj A, Nag S, Muddle BC, et al. Competing martensitic, bainitic, and pearlitic transformations in a hypoeutectoid Ti-5Cu alloy. *Metall Mater Trans A*. 2011;42(5):1139–1143.
- [165] Devaraj A, Kaspar TC, Ramanan S, et al. Nanoscale phase separation in epitaxial Cr-Mo and Cr-V alloy thin films studied using atom probe tomography: comparison of experiments and simulation. *J Appl Phys*. 2014;116(19):193512.
- [166] Nag S, Zheng Y, Williams REA, et al. Non-classical homogeneous precipitation mediated by compositional fluctuations in titanium alloys. *Acta Materialia*. 2012;60(18):6247–6256.

- [167] Nag S, Mahdak KC, Devaraj A, et al. Phase separation in immiscible silver-copper alloy thin films. *J Mater Sci.* **2009**;44(13):3393–3401.
- [168] Danoix F, Auger P, Blavette D. Hardening of aged duplex stainless steels by spinodal decomposition. *Microsc Microanal.* **2004**;10(3):349–354.
- [169] Zhou J, Odqvist J, Thuvander M, et al. Quantitative evaluation of spinodal decomposition in Fe-Cr by atom probe tomography and radial distribution function analysis. *Microsc Microanal.* **2013**;19(3):665–675.
- [170] Capdevila C, Miller MK, Russell KF, et al. Phase separation in PM 2000 (TM) Fe-base ODS alloy: experimental study at the atomic level. *Mat Sci Eng A-Struct.* **2008**;490(1–2):277–288.
- [171] Muller CM, Sologubenko AS, Gerstl SSA, et al. On spinodal decomposition in Cu-34 at % Ta thin films – an atom probe tomography and transmission electron microscopy study. *Acta Materialia.* **2015**;89:181–192.
- [172] Emo J, Pareige C, Sallet S, et al. Kinetics of secondary phase precipitation during spinodal decomposition in duplex stainless steels: a kinetic Monte Carlo model – comparison with atom probe tomography experiments. *J Nucl Mater.* **2014**;451(1–3):361–365.
- [173] Danoix F, Auger P. Atom probe studies of the Fe-Cr system and stainless steels aged at intermediate temperature: a review. *Mater Charact.* **2000**;44(1–2):177–201.
- [174] Puthucode A, Devaraj A, Nag S, et al. De-vitrification of nanoscale phase-separated amorphous thin films in the immiscible copper–niobium system. *Philos Mag.* **2014**;94(15):1622–1641.
- [175] Katakam S, Devaraj A, Bowden M, et al. Laser assisted crystallization of ferromagnetic amorphous ribbons: a multimodal characterization and thermal model study. *J Appl Phys.* **2013**;114(18):184901.
- [176] DeGeorge V, Devaraj A, Keylin V, et al. Mass balance and atom probe tomography characterization of soft magnetic $(\text{Fe}_{65}\text{Co}_{65})_{79.5}\text{B}_{13}\text{Si}_2\text{Nb}_4\text{Cu}_{1.5}$ nanocomposites. *IEEE Trans Magnet.* **2015**;51(6):1–4.
- [177] Jiang X, Devaraj A, Balamurugan B, et al. Microstructure of multistage annealed nanocrystalline $\text{SmCo}_2\text{Fe}_2\text{B}$ alloy with enhanced magnetic properties. *J Appl Phys.* **2014**;115(6):063902.
- [178] Oleksak RP, Devaraj A, Herman GS. Atomic-scale structural evolution of Ta–Ni–Si amorphous metal thin films. *Mater Lett.* **2016**;164:9–14.
- [179] Li X, Ma CT, Lu J, et al. Exchange bias and bistable magneto-resistance states in amorphous TbFeCo thin films. *Appl Phys Lett.* **2016**;108(1):012401.
- [180] Miller MK. Atom probe tomography characterization of solute segregation to dislocations. *Microsc Res Techniq.* **2006**;69(5):359–365.
- [181] Detor AJ, Miller MK, Schuh CA. Measuring grain-boundary segregation in nanocrystalline alloys: direct validation of statistical techniques using atom probe tomography. *Phil Mag Lett.* **2007**;87(8):581–587.
- [182] Toyama T, Nozawa Y, Van Renterghem W, et al. Grain boundary segregation in neutron-irradiated 304 stainless steel studied by atom probe tomography. *J Nucl Mat.* **2012**;425(1–3):71–75.
- [183] Seol JB, Lim NS, Lee BH, et al. Atom probe tomography and nano secondary ion mass spectroscopy investigation of the segregation of boron at austenite grain boundaries in 0.5 wt.% carbon steels. *Met. Mater. Int.* **2011**;17(3):413–416.
- [184] Miller MK, Hoelzer DT, Kenik EA, et al. Stability of ferritic MA/ODS alloys at high temperatures. *Intermetallics.* **2005**;13(3–4):387–392.
- [185] Miller MK, Russell KF. Embrittlement of RPV steels: an atom probe tomography perspective. *J Nucl Mater.* **2007**;371(1–3):145–160.
- [186] Cairney JM, Saxey DW, McGrouther D, et al. Site-specific specimen preparation for atom probe tomography of grain boundaries. *Physica B.* **2007**;394(2):267–269.
- [187] Kuzmina M, Ponge D, Raabe D. Grain boundary segregation engineering and austenite reversion turn embrittlement into toughness: example of a 9 wt.% medium Mn steel. *Acta Materialia.* **2015**;86:182–192.
- [188] Kelly TF, Larson DJ, Thompson K, et al. Atom probe tomography of electronic materials. *Annu Rev Mater Res.* **2007**;37:681–727.
- [189] Lai L. The strategy of advanced analysis in semiconductor nano-device: from nanoprobe to nanoscopy and nanoanalysis. *Microsc Microanal.* **2014**;20(Supplement S3):980–981.
- [190] Thompson K, Flaitz PL, Ronsheim P, et al. Imaging of arsenic Cottrell atmospheres around silicon defects by three-dimensional atom probe tomography. *Science.* **2007**;317(5843):1370–1374.
- [191] Ronsheim P, Flaitz P, Hatzistergos M, et al. Impurity measurements in silicon with D-SIMS and atom probe tomography. *Appl Surf Sci.* **2008**;255(4):1547–1550.
- [192] Lauhon LJ, Adusumilli P, Ronsheim P, et al. Atom-probe tomography of semiconductor materials and device structures. *MRS Bull.* **2009**;34(10):738–743.
- [193] Kim Y-C, Adusumilli P, Lauhon LJ, et al. Three-dimensional atomic-scale mapping of Pd in $\text{Ni}_{1-x}\text{Pd}_x\text{Si}/\text{Si}(100)$ thin films. *Appl Phys Lett.* **2007**;91(11):113106.
- [194] Larson D, Alvis R, Lawrence D, et al. Analysis of bulk dielectrics with atom probe tomography. *Microsc Microanal.* **2008**;14(Supplement S2):1254–1255.
- [195] Ulfig R, Thompson K, Alvis R, et al. Three dimensional compositional characterization of dielectric films with LEAP tomography. *Microsc Microanal.* **2007**;13(Supplement S02):828–829.
- [196] Inoue K, Yano F, Nishida A, et al. Dopant distributions in n-MOSFET structure observed by atom probe tomography. *Ultramicroscopy.* **2009**;109(12):1479–1484.
- [197] Larson DJ, Lawrence D, Lefebvre W, et al. Toward atom probe tomography of microelectronic devices. *J Phys Conf Ser.* **2011**;326.
- [198] Kambham AK, Mody J, Gilbert M, et al. Atom-probe for FinFET dopant characterization. *Ultramicroscopy.* **2011**;111(6):535–539.
- [199] Takamizawa H, Shimizu Y, Nozawa Y, et al. Dopant characterization in self-regulatory plasma doped fin field-effect transistors by atom probe tomography. *Appl Phys Lett.* **2012**;100(9):93502.
- [200] Han B, Takamizawa H, Shimizu Y, et al. Phosphorus and boron diffusion paths in polycrystalline silicon gate of a trench-type three-dimensional metal-oxide-semiconductor field effect transistor investigated by atom probe tomography. *Appl Phys Lett.* **2015**;107(2):23506.
- [201] Kambham AK, Kumar A, Gilbert M, et al. 3D site specific sample preparation and analysis of 3D devices (FinFETs) by atom probe tomography. *Ultramicroscopy.* **2013**;132:65–69.

- [202] Kambham AK, Zschaetzsch G, Sasaki Y, et al. Atom probe tomography for 3D-dopant analysis in FinFET devices. 2012 Symposium on VLSI Technology (VLSIT), 2012 Jun 12–14; 2012. p. 77–78.
- [203] Kambham AK, Kumar A, Florakis A, et al. Three-dimensional doping and diffusion in nano scaled devices as studied by atom probe tomography. *Nanotechnology*. **2013**;24(27):275705.
- [204] Panciera F, Hoummada K, Gregoire M, et al. Atom probe tomography of SRAM transistors: specimen preparation methods and analysis. *Microelectron Eng*. **2013**;107:167–172.
- [205] Hatzistergos MS, Hopstaken M, Kim E, et al. Characterization of 3D dopant distribution in state of the art FinFET structures. *Microsc Microanal*. **2013**;19(Supplement S2):960–961.
- [206] Grenier A, Duguay S, Barnes JP, et al. 3D analysis of advanced nano-devices using electron and atom probe tomography. *Ultramicroscopy*. **2014**;136:185–192.
- [207] Gilbert M, Vandervorst W, Koelling S, et al. Atom probe analysis of a 3D finFET with high-k metal gate. *Ultramicroscopy*. **2011**;111(6):530–534.
- [208] Koelling S, Innocenti N, Hellings G, et al. Characteristics of cross-sectional atom probe analysis on semiconductor structures. *Ultramicroscopy*. **2011**;111(6):540–545.
- [209] Silaeva EP, Karahka M, Kreuzer HJ. Atom probe tomography and field evaporation of insulators and semiconductors: theoretical issues. *Curr Opin Solid St M*. **2013**;17(5):211–216.
- [210] Joshi VV, Lavender C, Moxon V, et al. Development of Ti-6Al-4V and Ti-1Al-8V-5Fe alloys using low-cost TiH₂ powder feedstock. *J Mater Eng Perform*. **2013**;22(4):995–1003.
- [211] Agrawal R, Bernal RA, Isheim D, et al. Characterizing atomic composition and dopant distribution in wide band gap semiconductor nanowires using laser-assisted atom probe tomography. *J Phys Chem C*. **2011**;115(36):17688–17694.
- [212] Zhang SX, Hemesath ER, Perea DE, et al. Relative influence of surface states and bulk impurities on the electrical properties of Ge nanowires. *Nano Lett*. **2009**;9(9):3268–3274.
- [213] Eichfeld CM, Gerstl SSA, Prosa T, et al. Local electrode atom probe analysis of silicon nanowires grown with an aluminum catalyst. *Nanotechnology*. **2012**;23(21):215205.
- [214] Moutanabbir O, Isheim D, Blumtritt H, et al. Colossal injection of catalyst atoms into silicon nanowires. *Nature*. **2013**;496(7443):78–82.
- [215] Yu LW, Chen WH, O'Donnell B, et al. Growth-in-place deployment of in-plane silicon nanowires. *Appl Phys Lett*. **2011**;99(20):203104.
- [216] Allen JE, Hemesath ER, Perea DE, et al. High-resolution detection of Au catalyst atoms in Si nanowires. *Nat Nanotechnol*. **2008**;3(3):168–173.
- [217] Schlitz RA, Perea DE, Lensch-Falk JL, et al. Correlating dopant distributions and electrical properties of boron-doped silicon nanowires. *Appl Phys Lett*. **2009**;95:162101.
- [218] Yoon K, Hyun JK, Connell JG, et al. Barrier height measurement of metal contacts to Si nanowires using internal photoemission of hot carriers. *Nano Lett*. **2013**;13(12):6183–6188.
- [219] den Hertog MI, Schmid H, Cooper D, et al. Mapping active dopants in single Silicon nanowires using off-axis electron holography. *Nano Lett*. **2009**;9(11):3837–3843.
- [220] Connell JG, Yoon K, Perea DE, et al. Identification of an intrinsic source of doping inhomogeneity in vapor-liquid-solid-grown nanowires. *Nano Lett*. **2013**;13(1):199–206.
- [221] Perea DE, Hemesath ER, Schwalbach EJ, et al. Direct measurement of dopant distribution in an individual vapour-liquid-solid nanowire. *Nat Nanotechnol*. **2009**;4(5):315–319.
- [222] Schmitz G, Abouzari R, Berkemeier F, et al. Nanoanalysis and ion conductivity of thin film battery materials. *Z Phys Chem*. **2010**;224(10–12):1795–1829.
- [223] Diercks DR, Musselman M, Morgenstern A, et al. Evidence for anisotropic mechanical behavior and nanoscale chemical heterogeneity in cycled LiCoO₂. *J Electrochem Soc*. **2014**;161(11):F3039–F3045.
- [224] Devaraj A, Gu M, Colby R, et al. Visualizing nanoscale 3D compositional fluctuation of lithium in advanced lithium-ion battery cathodes. *Nat Commun*. **2015**;6:8014.
- [225] Santhanagopalan D, Schreiber DK, Perea DE, et al. Effects of laser energy and wavelength on the analysis of LiFePO₄ using laser assisted atom probe tomography. *Ultramicroscopy*. **2015**;148:57–66.
- [226] Bagot PAJ, Kreuzer HJ, Cerezo A, et al. A model for oxidation-driven surface segregation and transport on Pt-alloys studied by atom probe tomography. *Surf Sci*. **2011**;605(15–16):1544–1549.
- [227] Li T, Bagot PAJ, Marquis EA, et al. Characterization of oxidation and reduction of Pt-Ru and Pt-Rh-Ru alloys by atom probe tomography and comparison with Pt-Rh. *J Phys Chem C*. **2012**;116(33):17633–17640.
- [228] Li T, Bagot PAJ, Marquis EA, et al. Characterization of oxidation and reduction of a Palladium-Rhodium alloy by atom-probe tomography. *J Phys Chem C*. **2012**;116(7):4760–4766.
- [229] Li T, Bagot PAJ, Marquis EA, et al. Atomic engineering of platinum alloy surfaces. *Ultramicroscopy*. **2013**;132:205–211.
- [230] Bagot PAJ, Kruska K, Haley D, et al. Oxidation and surface segregation behavior of a Pt-Pd-Rh alloy catalyst. *J Phys Chem C*. **2014**;118(45):26130–26138.
- [231] Tedsree K, Li T, Jones S, et al. Hydrogen production from formic acid decomposition at room temperature using a Ag-Pd core-shell nanocatalyst. *Nat Nanotechnol*. **2011**;6(5):302–307.
- [232] Felfer P, Benndorf P, Masters A, et al. Revealing the distribution of the atoms within individual bimetallic catalyst nanoparticles. *Angew Chem Int Edit*. **2014**;53(42):11190–11193.
- [233] Kuchibhatla SVNT, Shutthanandan V, Prosa TJ, et al. Three-dimensional chemical imaging of embedded nanoparticles using atom probe tomography. *Nanotechnology*. **2012**;23:215704.
- [234] Vilayurganapathy S, Devaraj A, Colby R, et al. Subsurface synthesis and characterization of Ag nanoparticles embedded in MgO. *Nanotechnology*. **2013**;24:095707.
- [235] Perea DE, Arslan I, Liu J, et al. Determining the location and nearest neighbours of aluminium in zeolites with atom probe tomography. *Nat Commun*. **2015**;6:7589.
- [236] Devaraj A, Vijayakumar M, Bao J, et al. Discerning the location and nature of coke deposition from

- surface to bulk of spent zeolite catalysts. *Sci Rep.* **2016**;6:37586.
- [237] Dumpala S, Broderick SR, Bagot PAJ, et al. An integrated high temperature environmental cell for atom probe tomography studies of gas-surface reactions: instrumentation and results. *Ultramicroscopy.* **2014**;141:16–21.
- [238] Zinner EK, Moynier F, Stroud RM. Laboratory technology and cosmochemistry. *Proc Nat Acad Sci.* **2011**;108(48):19135–19141.
- [239] Heck PR, Pellin MJ, Davis AM, et al. Atom-probe tomographic analyses of presolar silicon carbide grains and meteoritic nanodiamonds – first results on silicon carbide. Lunar and Planetary Science Conference. Woodlands, Texas, 2010.
- [240] Stadermann FJ, Zhao X, Daulton TL, et al. Atom-probe tomographic study of the three-dimensional structure of presolar silicon carbide and nanodiamonds at atomic resolution. Lunar and Planetary Science Conference. Woodlands, Texas, 2010.
- [241] Stadermann FJ, Isheim D, Zhao X, et al. Atom-probe tomographic characterization of meteoritic nanodiamonds and presolar SiC. 42nd Lunar and Planetary Science Conference. The Woodlands, Texas, USA, 2011.
- [242] Daulton TL, Eisenhour DD, Bernatowicz TJ, et al. Genesis of presolar diamonds: comparative high-resolution transmission electron microscopy study of meteoritic and terrestrial nano-diamonds. *Geochimica et Cosmochimica Acta.* **1996**;60(23):4853–4872.
- [243] Heck PR, Pellin MJ, Davis AM, et al. Atom-probe tomography of meteoritic and synthetic nanodiamonds. *Meteorit Planet Sci.* **2011**;46:A90–A90.
- [244] Valley JW, Cavosie AJ, Ushikubo T, et al. Hadean age for a post-magma-ocean zircon confirmed by atom-probe tomography. *Nature Geoscience.* **2014**;7:219–223.
- [245] Parman SW, Gorman B, Jackson C, et al. Effect of laser power on atom probe tomography of silicates. American Geophysical Union, Fall Meeting. Denver, CO, USA, 2010.
- [246] Parman SW, Gorman B, Jackson C, et al. Atom probe tomography of olivine. American Geophysical Union, Fall Meeting. Denver, CO, USA, 2010.
- [247] Muller EW. Das Feldionenmikroskop. *Z Phys.* **1951**;131(1):136–142.
- [248] Abbott RC. Dc field desorption of macromolecules. *J Chem Phys.* **1965**;43(12): 4533.
- [249] Muller EW, Rendulic KD. Field ion microscopical imaging of biomolecules. *Science.* **1967**;156(3777):961–963.
- [250] Joester D, Hillier A, Zhang Y, et al. Organic materials and organic/inorganic heterostructures in atom probe tomography. *Microscopy Today.* **2012**;20(3):26–31.
- [251] Kelly TF, Nishikawa O, Panitz JA, et al. Prospects for nanobiology with atom-probe tomography. *MRS Bull.* **2009**;34(10):744–750.
- [252] Chasteen ND, Harrison PM. Mineralization in ferritin: an efficient means of iron storage. *J Struct Biol.* **1999**;126(3):182–194.
- [253] Panitz JA. Point-projection imaging of macromolecular contours. *J Microsc-Oxford.* **1982**;125(Jan):3–23.
- [254] Panitz JA. Point-projection imaging of unstained ferritin clusters. *Ultramicroscopy.* **1982**;7(3):241–247.
- [255] Greene ME, Kelly TF, Larson DJ, et al. Focused ion beam fabrication of solidified ferritin into nanoscale volumes for compositional analysis using atom probe tomography. *J Microsc-Oxford.* **2012**;247(3):288–299.
- [256] Gordon LM, Cohen MJ, Joester D. Towards atom probe tomography of hybrid organic-inorganic nanoparticles. *Microsc Microanal.* **2013**;19(Suppl. 2):2013.
- [257] Narayan K, Prosa TJ, Fu J, et al. Chemical mapping of mammalian cells by tom probe tomography. *J Struct Biol.* **2012**;178(2):98–107.
- [258] Marquis EA, Geiser BP, Prosa TJ, et al. Evolution of tip shape during field evaporation of complex multilayer structures. *J Microsc-Oxford.* **2011**;241(3):225–233.
- [259] Gordon LM, Joester D. Nanoscale chemical tomography of buried organic-inorganic interfaces in the chiton tooth. *Nature.* **2011**;469(7329):194–197.
- [260] Gordon LM, Tran L, Joester D. Atom probe tomography of apatites and bone-type mineralized tissues. *ACS Nano.* **2012**;6(12):10667–10675.
- [261] Karlsson J, Sundell G, Thuvander M, et al. Atomically resolved tissue integration. *Nano Lett.* **2014**;14(8):4220–4223.
- [262] Gordon LM, Cohen MJ, MacRenaris KW, et al. Amorphous intergranular phases control the properties of rodent tooth enamel. *Science.* **2015**;347(6223):746–750.
- [263] Gordon LM, Joester D. Mapping residual organics and carbonate at grain boundaries and in the amorphous interphase in mouse incisor enamel. *Front Physiol.* **2014**;5:509.
- [264] Xu Z, Li D, Xu W, et al. Simulation of heterogeneous atom probe tip shapes evolution during field evaporation using a level set method and different evaporation models. *Comput Phys Commun.* **2015**;189: 106–113.